UNIVERSITY OF CALIFORNIA
RIVERSIDE

Thermal Management Using Graphene and Carbon-Nanotubes

A Dissertation submitted in partial satisfaction
of the requirements for the degree of

Doctor of Philosophy

in

Materials Science and Engineering

by

Pradyumna Goli

March 2014

Dissertation Committee:
Dr. Alexander A. Balandin, Chairperson
Dr. Roger K. Lake
Dr. Alexander A. Khitun

The Dissertation of Pradyumna Goli is approved:

_____

_____

_____

Committee Chairperson

University of California, Riverside

Acknowledgements

It gives me great pleasure to take this opportunity to acknowledge all the people who supported me in the last several years during my PhD here at UC Riverside.

Firstly, and most importantly, I would like to express the deepest appreciation to my committee chair, Professor Alexander A. Balandin, who has the attitude and the substance of a genius: he continually and convincingly conveyed a spirit of adventure in regard to research. Without his guidance, support and persistent help this dissertation would not have been possible. His research standards, intensity and dedication to science gave me freedom and opportunities to explore challenging research areas.

I would like to thank my committee member, Professor Roger Lake and Professor Alexander Khitun, without whom I wouldn't be able to complete my PhD. I would also like to take this opportunity to thank the Bill Bingham, Maggie Souders and Trudi Loader for their wonderful guidance and assistance during the program.

I am heartily thankful to Dr. Javed M. Khan, Friend, Family and Guide, whose encouragement, guidance and support from the initial to the final level enabled me to develop strength to take any project. The countless emails and telephone conversations he spent in discussions with me have been an invaluable experience for me.

I thank Sir. Konstantin S. Novoselov, Manchester University, and Dr. Chung Ping Lai, CEO of Bluestone Global Tech for providing CVD grown graphene samples for thermal conductivity measurements. I am blessed to work with them very closely.

I appreciate the financial support from SRC-DARPA through STARnet center on Function Accelerated nanoMaterial Engineering Center (FAME) and NRI-NSF nano 2020 grant. I thank my fellow labmates in UCR NDL Group: Dr. Goyal, Dr. Hossain, Dr. Amini, Dr. Calizo, Dr. Gosh, Dr. Kotchetkov, Dr. Teweldebrhan, Dr. Nolen, Dr. Rehman, Dr. Bejenari, Dr. Subrina, Dr. Yu, Dr. Liu, Dr. Yan, Dr. Shahil, Stanislav Legedza, Ruben Salgado, Aditya Dhar, Chenglong Jiang, Rameez Samnakay, Dr. Renteria, Hoda Malekpur, Sylvester Ramirez, Frederick Gertz, Darshana Wickramaratne, Mahesh Neupane, Gen Yin, and my friends Behlul Sutarwala, Ashrit Rohit for the encouragement, support and for all the fun we have had in the last five years. Particularly I would like to extend my sincere heartfelt thanks to my long standing buddies Dhananjay Ipparthi, Rahul Potharaju and Dr. Anil Potharaju, without whom I would not have survived through the extreme moments of stress.

I would also like to thank my relatives and cousins, particularly I would like to thank Venukumari, G K Mohan, Anu, Sree, Abinay, Hima Bindu, Srinivas, Praveen, Haritha, Avanthi and Ravi, for helping me and supporting me in every possible way they can and making my stay at UCR very easy, enjoyable and memorable.

Last but not the least, I would like to thank my family: my parents Dr G V Bhavani Prasad and Vijaya Laxmi Goli, for giving birth to me at the first place and supporting me throughout my life, I will never forget the sacrifices they made for me. My brother G Kalyan Raghav, for teaching me how to face challenges in life and my sister Pratyusha Goli for being a caring sister. This work would not have been possible without steadfast support and encouragement of my wife Mrs. Divya Perumandla. Their unflinching courage and conviction will always inspire me, and I hope to continue, in my own small way. It is to them that I dedicate this work.

The text of this dissertation in part of full, is a reprint of the material as it appears in the following Journals:

- P. Goli, S. Legedza, A. Dhar, R. Salgado, J. Renteria and A. A. Balandin, "Graphene-enhanced hybrid phase change materials for thermal management of Li-ion batteries", Journal of Power Sources 248 (1), 37 (2014).

- P. Goli, X. Li, C. Y. Lu, K. S. Novoselov and A. A. Balandin, Strong Enhancement of Thermal Properties of Copper Films after Chemical Vapor Deposition of Graphene", Nanoletters, ASAP, 2014.

Dedicated to my parent
and
my wife

ABSTRACT OF THE DISSERTATION

Thermal Management Using Graphene and Carbon-Nanotubes

by

Pradyumna Goli

Doctor of Philosophy, Graduate Program in Materials Science and Engineering
University of California, Riverside, March 2014
Professor Alexander A. Balandin, Chairperson

This dissertation investigates the application of graphene and carbon nanotubes (CNTs) for thermal management of high-power batteries and interconnects. The research is focused on three applications: (i) thermal phase change materials (PCMs) with graphene fillers for thermal management of battery packs; (ii) CNTs incorporated in the battery electrodes; (iii) graphene coatings for copper (Cu) interconnects. In this study, lithium-ion (Li-ion) batteries were used for testing the proposed approaches. The graphene solutions for synthesis of graphene PCMs were obtained by the liquid-phase exfoliation. The graphene coatings on Cu films were grown by the chemical vapor deposition (CVD). In the first part of the dissertation, it is demonstrated that thermal management of Li-ion batteries can be drastically improved using PCM with graphene fillers. Incorporation of graphene to the hydrocarbon-based PCM allowed one to increase its thermal conductivity by more than *two orders of magnitud*e while preserving its latent heat storage ability. A combination of the sensible and latent heat storage together with the improved heat

conduction outside of the battery pack leads to a significant decrease in the temperature rise inside the Li-ion battery pack. I the second part of the dissertation, it is shown that thermal properties of Li-ion battery electrodes can be improved by incorporation of CNTs. The electrodes were synthesized via an inexpensive *scalable filtration method*, which can be extended to commercial electrode-active materials. The measurements reveal that the in-plane (cross-plane) thermal conductivity of the cathodes with the highest battery capacity was ~50 W/mK (3 W/mK) at room temperature. These values are up *to two-orders-of-magnitude* higher than those for conventional electrodes based on carbon black. The highest in-plane thermal conductivity achieved in the carbon-nanotube-enhanced electrodes was ~141 W/mK. In third part of the dissertation, it is demonstrated that graphene coating can strongly increase the thermal conductivity of Cu films as compared to the reference Cu and annealed Cu films. The observed improvement of thermal properties of graphene coated Cu films results primarily from the changes in Cu morphology during graphene CVD rather than from graphene's action as an additional heat conducting channel. The obtained results are important for thermal management of advanced batteries and downscaled computer chips.

Contents

List of Figure

Chapter I

Introduction

1.1. Thermal Management of Li-Ion Batteries

The world energy market will demand energy densities of 35.2 trillion kWh by 2035 which is a 31% increase in consumption from 2011 [1]. The United States currently imports 30% of its energy to meet the present electricity demands consumed domestically since domestic consumption exceeds production [2]. To address the energy generation and storage needs, the Department of Energy (DOE), Federal Energy Regulatory Committee (FERC) and National Institute of Standards (NIST) have detailed an energy roadmap to reduce our foreign dependency on energy while increasing the demand of renewable energies [3-5]. This initiative articulates a national energy portfolio which will increase the production of renewable electric energies from photovoltaic, wind, wood, biofuels and hydroelectrics to create a utility scale energy generation and storage for a smart grid system which will support a large scale plug-in electric vehicle system. In addition to the current technologies, there are emerging renewable energy resources such as thermoelectric and ocean devices entering the global energy market [6-7]. The demand for renewable energies will be created by (1) enabling utility systems and private facilities to utilize renewable sources of energy local and through grid distribution, (2) create a large scale electric transportation for the growing plug-in electric vehicles (EV). Since the utility grid distribution varies based on demand while EVs require rechargeable batteries to generate and store the energy based on usage, the need for high performance and long term storage will be required for high power densities to supply electricity to the grid and high energy densities for long term operation of EVs.

Development of Lithium-ion (Li-ion) batteries enabled progress in mobile communications, consumer electronics, automotive and aerospace industries. Li-ion batteries are an essential part of the hybrid electric vehicles (HEV) owing to their high energy densities and low weight-to-volume ratios [8]. One of the most significant factors negatively affecting Li-ion battery performance is a temperature rise beyond the normal operating range. If overheated due to short-circuiting or fast charging/discharging processes the Li-ion battery can suffer thermal runaway, cell rupture or even explosion [9]. A fire in the Li-ion battery results in the emission of dense irritating smoke which could present a serious health and environmental risk [10]. Combining multiple Li-ion cells close together in a battery pack in order to provide higher electric power makes the thermal management of the batteries even more challenging. The severity of the potential thermal issues with the battery packs is exemplified by a recent incident with the overheating and fire in the batteries on-board the Boeing 787 Dreamliner [11].

1.2. Thermal Management at Nano-Scale

The invention of solid state transistor and subsequent invention of the integrated circuit (IC) has advocated an unparallel technological and economic growth. In the last one decade, the aggressive downscaling of the device size has yielded enormous gains in terms of speed, energy efficiency, portability, device density and form factor. So far, device engineers have been successful to maintain Moore's Law, which states that the numbers of transistors on an integrated chip will double every year [12]. This law was predicted to last a decade, from 1965 to 1975. In 1975, this slope changed to doubling

every 18 months. This has led to both a reduction of the size of transistors as well as an increase in the packing density. The increase in transistor density has also leaded to a significant increase in the power density (heat) in the same area that needs to be removed from the chip [13]. This law has continued for almost half a century and in 2005 was not expected to stop for another decade at least, because the fundamental thermodynamic limits are being reached in critical areas and innovative changes need to be made in both device structures and transistor materials so that the current rate of improvement can be maintained. The variety of novel phenomena that emerge at nanoscale include spatial confinement and quantization of phonon modes [14], decreased phonon group velocity, increased phonon boundary scattering [15], phonon redistribution due to scattering from rough boundaries and interfaces, pronounced thermal boundary resistance, and rarefied phonon gas effect. When the device feature size becomes comparable to the phonon mean-free-path (MFP) then in addition to the Umklapp scattering and Rayleigh scattering, phonon boundary/rough interface scattering emerges as a dominant phonon scattering mechanism. The definition of temperature also becomes very crucial in the scale of phonon mean free path and wavelength [16].

Thermal management has traditionally been a post-chip-making effort. Currently, it starts from the device and circuits packaging level itself. Increased number of interconnects and decreased transistor feature size lead to an increased thermal resistance of the ICs and the associated difficulties in heat removal [17]. Another phenomenon, which becomes more crucial as photonic device integration increases and the number of layers go up, is the thermal boundary resistance. It occurs when the heat flows in the direction normal to the

interface of two materials, a temperature drop may develop due to the acoustic impedance mismatch between the two materials even if the interface is atomically sharp [18].

Another aspect of the nanoscale heat management is related to the increasing demand of the operating speed of electronic devices. Effective means of heat removal are becoming a pressing issue for assuring the reliable performance and longevity of the nanodevices. Detailed knowledge of the mechanisms and physics in heat dissipation is thus essential for assuring superior thermal performance of nanodevices.

1.3. Thermal Boundary Resistance

Thermal boundary resistance (TBR) is defined as the inverse of thermal conductance, G, and it is used to describe thermal transport across an interface. TBR is given by

$$R_{Bd} = \left[\frac{\dot{Q}}{A.\Delta T}\right] \qquad [1.1]$$

where $\dot{Q}$ is the heat flow across an interface, A is the unit area and ΔT is the temperature difference between the two sides of the interface. When heat is transferred across an interface between two different materials, there is a temperature discontinuity at the interface. This effect was first observed at the interface between metal and liquid helium [19] but has later also been seen at the interface between two solids [20]. The qualitative differences between the behavior of boundary resistances at solid-solid and solid-helium interfaces can be explained by two limiting models of boundary resistance, the acoustic mismatch model – which assumes no scattering and the diffuse mismatch model – which

assumes that all phonons incident on the interface will scatter. The qualitative differences between the behavior of boundary resistances at solid-solid and solid-helium interfaces can be explained by two limiting models of boundary resistance, the acoustic mismatch model which assumes no scattering and the diffuse mismatch model which assumes that all phonons incident on the interface will scatter.

Thermal boundary resistance at solid-solid interface plays an important role in the thermal stability of many electronic circuits, micro devices, superconducting devices, and the whole package itself. With the ever-decreasing size of microelectronics, growing applications of super lattices, and development of nanotechnology, effect of thermal resistances between interfaces (solid-solid) on thermal conductivity are becoming increasingly important. In 1952, the first theoretical description of the phenomenon was suggested by Khalatnikov [21]. The description, currently known as the acoustic mismatch model (AMM), predicts poor phonon transport across interfaces when there are large differences in the density and sound velocity for the two interface materials, as is the case for the interface between liquid helium and most solids. The AMM was extended to solid-solid interfaces by Little in 1959 [12]. More recently, in 1987, Swartz measured TBR for several metal film and dielectric interfaces up to a temperature of 200 K [22]. Swartz found that below 30 K there was good agreement between the model and experiment, but above 30 K the model tended to under predict the measured TBR.

In order to account for the phonon scattering at interfaces, the diffuse mismatch model (DMM) was suggested by Swartz and Pohl [14]. The model assumes that all phonons

incident on the interface from both sides are elastically scattered and then are emitted to either side of the interface. The probability for a phonon to be emitted to a particular side is proportional to the phonon density of states (DOS) of the two materials. Inherent to the DMM is that the transport is independent of the interface structure itself and is only dependent on the properties of the two materials. DMM also assumes only elastic scattering takes place at the interface. In the case of low temperature liquid He to solid interfaces the DMM predicts TBR two orders of magnitude lower than the one predicted by the AMM, while for solid-solid interfaces the differences are small [22]. Graphite nucleation

1.4. Overview

The introduction thus far suggests that in order to deal with the problem of increasing thermal issues in high density battery packs and hot spot temperatures in scaled down chips and devices, it is crucial to investigate thermal properties of materials at nanometer scale and identify materials and structures in which thermal properties can be engineered. This dissertation explores the thermal transport in a set of advanced engineered materials and device structures at nanoscale. We begin with the discussion of material properties and device structures investigated in this dissertation (Chapter 2). Chapter 3 discusses the experimental techniques used for thermal conductivity measurements which include two transient plane source techniques and the Raman optic technique. The first metrology tool discussed is the transient plane source (TPS) “hot disk” technique, which can measure the average in-plane thermal conductivity, and the second technique is the optical “laser

flash" technique (LFT), which measures the average cross-plane thermal conductivity. Raman optic technique was first developed for measurement of thermal conductivity of graphene [23]. This chapter describes the theory related to each experimental techniques used, the experimental set-up and the sample preparation procedure. In Chapter 4, experimental and theoretical results of thermal conduction in hybrid phase change materials with graphene as fillers. We show that thermal management and the reliability of Li-ion batteries can be drastically improved using hybrid phase change material with graphene fillers. Conventional thermal management of batteries relies on the latent heat stored in the phase change material as its phase changes over a small temperature range, thereby reducing the temperature rise inside the battery. Incorporation of graphene to the hydrocarbon-based phase change material allows one to increase its thermal conductivity by more than two orders of magnitude while preserving its latent heat storage ability. A combination of the sensible and latent heat storage together with the improved heat conduction outside of the battery pack leads to a significant decrease in the temperature rise inside a typical Li-ion battery pack. The described combined heat storage - heat conduction approach can lead to a transformative change in thermal management of Li-ion and other types of batteries. In chapter 5 we studied the thermal conductivity of Carbon-Nanotube enhanced Li-Ion battery electrodes for thermal management of Li-ion and other high-power-density batteries. In chapter 6, we demonstrated experimentally that graphene – Cu – graphene heterogeneous films reveal strongly enhanced thermal conductivity as compared to the reference Cu and annealed Cu films. Chemical vapor deposition of a single atomic plane of graphene on both sides of 9-μm-thick Cu films

increases their thermal conductivity by up to 24% near room temperature. Interestingly, the observed improvement of thermal properties of graphene – Cu – graphene hetero-films results primarily from the changes in Cu morphology during graphene deposition rather than from graphene's action as an additional heat conducting channel. Enhancement of thermal properties of graphene capped Cu films is important for thermal management of advanced electronic chips and proposed applications of graphene in the hybrid graphene – Cu interconnect hierarchies.

1.5. References

[1] J. Conti, P. Holtberg. 2011.

[2] U.S. Energy Information Administration. 2010.

[3] U. S. Department of Energy. 2011.

[4] U.S. Federal Energy Regulatory Commission. 2009. Docket No. PL09-4-000.

[5] U.S. Department of Commerce and National Institute of Standards and Technology 2010.

[6] G. J. Snyder and E. S. Toberer. Nat., 7, 2008.

[7] The California Energy Commision.

[8] Linden, D., Reddy, B.T. (2002) Handbook of Batteries. McGraw-Hill, New York.

[9] Spotnitz, R., Franklin, J. (2003) Abuse behavior of high-power, lithium-ion cells. Journal of Power Sources (Elsevier) 113, 81–100.

[10] Mikolajczak, C., Kahn, M., White, K., Long, R.T. (2011) Lithium-Ion Batteries Hazard and Use Assessment. Fire Protection Research Foundation, 76, 90, 102.

[11] FAA Press Release. (2013) Federal Aviation Administration. January 16.

[12] G. E. Moore, "Cramming More Components onto Integrated Circuits," Proc. of the IEEE, 86, 82-85, 1998.

[13] E. Pop, S. Sinha, and K. E. Goodson, "Heat Generation and Transport in Nanometer-Scale Transistors, Proc. of the IEEE, 94, 1587, 2006.

[14] A. A. Balandin and K. L. Wang, "Effect of phonon confinement on the thermoelectric figure of merit of quantum wells," J. of Appl. Phys., 84, 6149–6153, 1998.

[15] Chen, G., "Size and Interface Effects on Thermal Conductivity of Superlattices and Periodic Thin-Film Structures," J. of Heat Transfer, 119, 220, 1997.

[16] D. G. Cahill, W. K. Ford, K. E. Goodson, G. D. Mahan, A. Majumdar, H. J. Maris, R. Merlin, and S. R. Phillpot, "Nanoscale thermal transport," J. of Appl. Phys., 93, 793–818, 2003.

[17] A. A. Balandin, "New Materials and Designs can Keep Chips Cool," invited feature, IEEE Spectrum, 29-33, October 2009.

[18] W. A. Little, "The Transport of Heat between Dissimilar Solids at Low Temperatures," Canadian J. of Phys., 334-349, 1959.

[19] P. L. Kapitza, "The Study of Heat Transfer in Helium II," J. of Phys. USSR, 4, 181, 1941.

[20] E. T. Swartz and R. O. Pohl, "Thermal Boundary Resistance", Rev. Mod. Phys., 61, 605–667, 1989.

[21] I. M. Khalatnikov and I.N. Adamenko, "Theory of the Kapitza temperature discontinuity at a solid body-liquid helium boundary," Soviet Phys. JETP 36, 391-387, 1973.

[22] E. T. Swartz and R. O. Pohl, "Thermal Resistance at Interfaces," Appl. Phys. Lett. 51, 2200-2202, 1987.

[23] A. A. Balandin, S. Ghosh, W. Bao, I. Calizo, D. Teweldebrhan, F. Miao and C. N. Lau, "Superior thermal conductivity of single-layer graphene," Nano Lett. 8, 902-907, 2008.

Chapter II

2. Thermal Engineering in Advance Materials

2.1. Introduction

Thermal management is a critical issue for the energy and electronics industry. To prevent batteries and circuits from overheating and eventual breakdown, efficient heat removal techniques are necessary. Using materials with high thermal conductivities allows to increase the rate at which the heat can be transferred away from the devices and circuits. On the other hand materials with very low thermal conductivity are the focus of recent quest for high-efficiency thermoelectric materials. So, materials with both very high and very low thermal conductivities are technologically important. For this reason, it is important to investigate thermal properties of materials at nanometer scale and identify materials with the extremely large or extremely low thermal conductivity for applications as heat spreaders or heat insulators. Carbon has attracted much attention owing to its uniquely wide range of thermal conductivity. The various allotropes of carbon and their derivatives cover a wide range of thermal conductivity values from as low as 0.1 W/mK in diamond like carbon (DLC) [1] to above 5000 W/mK in single layer graphene [2-3]. Most of the heat in carbon materials is carried by lattice vibrations, i.e. acoustic phonons. The thermal conductivity of carbon materials depends on the structural disorder, sp^3 or sp^2 content of the material system, thickness and grain size of the films, and also on the dimensionality of the material system [4].

2.1.1. Graphene

Graphite has been known to have one of the highest thermal conductivity ~2000 W/mK in in-plane direction amongst carbon based materials [5]. After discovery of carbon nanotubes (CNT), one-dimensional form of carbon [6], several research groups reported very high thermal conductivity in CNTs, higher than those of graphite [7-8]. Measured thermal conductivity of an isolated multi walled CNT (MWCNT) were reported to be ~ 3000 W/mK around RT [9]. Berber et al. [10] theoretically reported a very high value of ~ 6600 W/m K using molecular dynamic simulations. More recently, Andre Geim and Konstantin Novoselov discovered graphene - a single isolated layer of sp^2 hybridized carbon atoms arranged in a honeycomb lattice, for which they split the 2010 Nobel Prize in Physics [11-14]. Graphene was first isolated by micromechanical cleavage of bulk graphite [11] and exhibits a bunch of unique electrical and thermal properties [11, 2-3]. Balandin et al. [2] used a Raman spectroscopy based technique to measure the thermal conductivity of this truly two dimensional system - graphene, and reported thermal conductivity values ~ 5000 W/mK which are on the higher end of that reported for CNTs. Graphene's unique properties make it a realistic candidate for a number of electronic applications. One major problem is that the micromechanically cleavage technique allows only minute quantities of graphene which may be sufficient for fundamental research but is unlikely to become commercially viable. There has been rapid progress in alternative routes to produce large area graphene which includes chemical vapor deposition [15-16], epitaxial growth of graphene on electrically insulating substrates [17], reduction of graphene derivatives such as graphene oxide [18-19]. These films are not single crystal

graphene and do not have thermal conductivity as high as single layer suspended graphene, but at the same time, they are much easier for synthesis in mass quantities and may find commercial applications.

2.2. Phase Change Materials

There is a call for improved phase change metarials (TIMs) which facilitate heat transfer across interface by reducing the contact resistance between the heat-generating batteries and heat-sinking units. The selection of a suitable PCM material to fill the interface between a batteries and a heat sink is critical to the performance and reliability of the battery packs. A common approach for thermal management of Li-ion battery packs is based on the utilization of phase-change materials (PCM). The latent heat stored in PCM, as its phase changes over a small temperature range, allows one to reduce the temperature rise inside the battery [20-23]. By varying the chemical composition of PCM one can tune its melting point and the temperature range in which it can operate as a heat absorber. It is important to note that common PCMs are characterized by very low thermal conductivity, K, with typical values in the range of 0.17 – 0.35 W/mK at room temperature (RT) [24]. For comparison, the RT thermal conductivity of silicon and copper are ~145 W/mK and ~381 W/mK, respectively. PCMs store heat from the batteries rather than transfer it away from the battery pack. The use of PCM in battery cells also serves the purpose of buffering the Li-ion cell from extreme fluctuations in ambient temperature. This is a different approach from what is used in the thermal management of computer chips. In order to reduce the temperature rise in a computer

chip one uses thin layers of thermal interface materials (TIMs) or heat spreaders that transfer heat from the chips to heat sinks and outside packaging [25-27]. The thermal conductivity of TIMs is in the range of 1 – 25 W/mK while that of solid graphite-based heat spreaders can be on the order of 103 W/mK [28].

Chapter 5 is dedicated to the experimental results on thermal conductivity of hybrid PCM's with graphene fillers. A number of disk-shaped samples were prepared by dispersion (via high-shear mixing) of aqueous graphene solution in to the paraffin wax. Graphene is known to have extremely high intrinsic thermal conductivity [29-30] and form excellent binding with a variety of matrix materials [27, 31-32]. The graphene-enhanced hybrid PCM reveals thermal conductivity that is two orders of magnitude higher than that of conventional PCM while preserving its latent heat storage ability. Utilization of the hybrid PCM results in substantial decrease of the temperature rise inside battery packs as demonstrated under realistic conditions.

2.3. References

[1] L. E. Bell, "Cooling, heating, generating power, and recovering waste heat with thermoelectric systems", Science, 321, 1457-1461, 2008.

[2] G. J. Snyder and E. S. Toberer, "Complex thermoelectric materials" Nat. Mater. 7, 105-114, 2008.

[3] C. J. Vineis, A. Shakouri, A. Majumdar and M. G. Kanatzidis, "Nanostructured Thermoelectrics: Big Efficiency Gains from Small Features", Adv. Mater. 22, 3970-3980 2010.

[4] K. Biswas, J. Q. He, I. D. Blum, C. I. Wu, T. P. Hogan, D. N. Seidman, V. P. Dravid and M. G. Kanatzidis, "High-performance bulk thermoelectrics with all-scale hierarchical architectures', Nature 489, 414-418, 2012.

[5] B. T. Kelly, "Physics of Graphite," Appl. Sc. Publishers, London, 1986.

[6] S. Ijima, "Helical Microtubules of Graphitic Carbon", Nature vol. 354, 56-58, 1991.

[7] R. S. Ruoff and D. C. Lorents, "Mechanical and Thermal Properties of Carbon Nanotubes", Carbon 33, 925-930, 1995.

[8] C. Yu, L. Shi, Z. Yao, D. Y. Li, and A. Majumdar, "Thermal Conductance and Thermopower of an Individual Single-wall Carbon Nanotube", Nano Lett., 5, 1842-1846, 2005.

[9] P. Kim, L. Shi, A. Majumder and P. L. McEuen, "Thermal Transport Measurements of Individual Multiwalled Nanotubes", Phys. Rev. Lett., 87, 215502, 2001.

[10] S. Berber, Y. K. Kwon, and D. Tomanek, "Unusually High Thermal Conductivity of Carbon Nanotubes", Phys. Rev. Lett. 84, 4613-4616, 2000.

[11] K. S. Novoselov, A. K. Geim, S. V. Morozov, D. Jiang, D. Zhang, S. V. Dubonos, I. V. Grigorieva, and A. A. Firsov, "Electric Field Effect in Atomically Thin Carbon Films", Science 306, 666-669, 2004.

[12] K. S. Novoselov, A. K. Geim, S. V. Morozov, D. Jiang, M. I. Katsnelson, I. V. Grigorieva, S. V. Dubonos, and A. A. Firsov, "Two-dimensional Gas of Massless Dirac Fermions in Graphene", Nature, 438, 197197–197200, 2005.

[13] A. K. Geim and K. S. Novoselov, "The Rise of Graphene", Nature Mat. 6, 183-191, 2007.

[14] http://nobelprize.org/nobel_prizes/physics/laureates/2010/press.html

[15] M. Eizenberg and J. M. Blakely, "Carbon Monolayer Phase Condensation on Ni(111)", Surface Sc., 82, 228–236, 1970.

[16] T. Aizawa, R. Souda, S. Otani, Y. Ishizawa and C. Oshima, "Anomalous Bond of Monolayer Graphite on Transition- Metal Carbide Surfaces", Phys. Rev. Lett., 64, 768–771, 1990.

[17] C. Berger, Z. Song, X. Li, X. Wu, N. Brown, C. Naud, D. Mayou, T. Li, J. Hass, A. N. Marchenkov, E. H. Conrad, P. N. First and W. A. De Heer, "Electronic Confinement and Coherence in Patterned Epitaxial Graphene", Science, 312, 1191–1196, 2006.

[18] S. Stankovich, R. D. Piner, S. T. Nguyen and R. S. Ruoff, "Synthesis and Exfoliation of Isocyanate Treated Graphene Oxide Nano-platelets", Carbon, 44, 3342–3347, 2006.

[19] S. Stankovich, R. D. Piner, X. Chen, N. Wu, S. T. Nguyen and R. S. Ruoff, "Stable Aqueous Dispersions of Graphitic Nanoplatelets via the Reduction of Exfoliated Graphite Oxide in the Presence of Poly (sodium 4-styrenesulfonate)", J. of Mat. Chem., 16, 155–158, 2006.

[20] P. Blake, P. D. Brimicombe, R. R. Nair, T. J. Booth, D. Jiang,F. Schedin, L. A. Ponomarenko, S. V. Morozov, H. F. Gleeson, E. W. Hill, A. K. Geim and K. S. Novoselov, "Graphene-based liquid crystal device", Nano Lett.,. 8, 1704-1708, 2008.

[21] B. Zalba, J. M. .Marin, and L. F. Cabeza, "Review on thermal energy storage with phase change: materials, heat transfer analysis and applications", Applied Thermal Engineering 23, 3, 251, 2003.

[22] F. Agyenim, N. Hewitt, P. Eames and S. Mervyn, "A review of materials, heat transfer and phase change problem formulation for latent heat thermal energy storage systems (LHTESS)" Renewable and Sustainable Energy Review 14, 615, 2010.

[23] M. M. Farid, A. M. Khudhair, S. A. Razack, Sand S. Al-Hallaj, "A review on phase change energy storage: materials and applications", Energy Conversion and Management 45, 1597, 2004.

[24] S. D. Sharma, and K. Sagara, "Latent heat storage materials and systems: A Reveiew", J. Green Energy, 2, 1, 2005.

[25] S. V. Garimella, A. S.Fleischer, J. Y. Murthy, A. Keshavarzi, R. Prasher, C. Patel, S. H. Bhavnani, R. Venkatasubramanian, R.Mahajan, Y. Joshi, B. Sammakia, B. A. Myers, L. Chorosinski, M. Baelmans, P. Sathyamurthy and P. E. Raad,

"Thermal Challenges in Next-Generation Electronic Systems", IEEE Trans. Compon. Packag. Technol, 31, 801−815, 2008.

[26] R. Prasher, "Thermal conductivity of composites of aligned nanoscale and microscale wires and pores", Proc. IEEE, 94, 1571−1585, 2006.

[27] K. M. F. Shahil and A. A. Balandin, "Graphene - multilayer graphene nanocomposites as highly efficient thermal interface materials", Nano Letters, 12, 861, 2012.

[28] A. Yan, G. Liu, J. M. Khan and A. A. Balandin, "Graphene quilts for thermal management of high-power GaN transistors", Nature Communications, 3, 827, 2012.

[29] A. A. Balandin, "Thermal properties of graphene and nanostructured carbon materials", Nature Materials, 10, 569 – 581, 2011.

[30] D. L. Nika and A. A. Balandin, "Two-dimensional phonon transport in graphene", Journal of Physics: Condensed Matter, 24, 233203, 2012.

[31] V. Goyal and A. A. Balandin, "Thermal properties of the hybrid graphene-metal nano-micro-composites: Applications in thermal interface materials", Applied Physics Letters, 100, 073113, 2012.

[32] K. M. F. Shahil and A. A. Balandin, "Thermal properties of graphene and multilayer graphene: Applications in thermal interface materials", Solid State Communications, 152, 1331, 2012.

Chapter III

Experiment Methodology

3.1. Introduction

In this chapter, the experimental methodology to study the thermal transport in advanced engineered materials is described. A complete theoretical background of the experimental technique has been provided. The chapter discusses the method of sample preparation for the experimental measurements and also describes the experimental setup. Several practical considerations, from sample size requirement to the elimination of thermal contact resistance, will also be discussed.

3.2 Transient Plane Source (TPS) "Hot Disk" Thermal Conductivity Measurement Technique

Hot Disk is a transient technique for thermal studies on various sample types was first proposed by Gustaffson [1]. Hot Disk is designed to non-destructively measure thermal conductivity and thermal diffusivity of solid, fluid and powder materials as well as materials with anisotropic thermal properties. The thermal transport properties of solids vary extensively depending on the structure, pressure, temperature, density, etc., of different materials. The main motive behind the development of the TPS technique has been to include large ranges of the transport properties and also to apply the same technique to large variety of materials [2]. The Hot Disk Thermal Constants Analyzer can be used for measuring thermal properties of a large variety of materials with thermal conductivities ranging from 0.005 W/mK to 500 W/mK over a wide temperature range.

The prime component in the Hot Disk system is the sensor (probe). The most compact and convenient sensor for measurements is the plane one, comprising a bifilar spiral. With this design the area of the sensor is minimized while the electrical resistance can be made comparatively large. The Hot Disk sensor probe comprises a flat resistive element with a continuous double-spiral of electrically-conducting nickel (Ni) metal etched out of thin foil and sandwiched between two layers of Kapton to provide both electrical insulation from the sample and mechanical stability for the sensor. The Nickel foil is chosen because of its high and well-known temperature coefficient of resistivity (TCR). This coil has a temperature coefficient (TCR) which can be deduced accurately for resistance recording. This nickel spiral is supported on both sides with a thin electrically insulating material. In TPS method, this electrically insulated flat nickel sensor plays a role of the heater and thermometer simultaneously. It is placed between two pieces of a sample under investigation. During the experiment, a constant current pulse is passed through the sensor, which generates heat. The heat generated dissipates through the sample on either side at a rate dependent on the thermal transport properties of the surrounding material. The temperature increase in the sensor is accurately determined through resistance measurement. Thermal properties of the material can be accurately determined by recording temperature rise as a function of time in the sensor. Fig. 3-1 shows the nickel bifilar sensor.

Nickel metal can be used as a sensor material over a large temperature range. In experiments performed with the Hot Disk, it can be used from 250 K to 700 K. However, it is not possible to use the same insulating material to support the Nickel spiral

throughout this temperature range. From cryogenic temperatures to about 500 K thin Kaptan films with a thickness of 12.7 μm or 25 μm, is being used. This gives a total thickness of the sensor between 60μm and 80μm. For measurements from 500 K to 1000 K Mica insulation, with a thickness of around 0.1mm, is being used, making the total thickness of the sensor about 0.25mm. To accommodate a broad range of materials and sample sizes, a wide selection of sensor sizes is available.

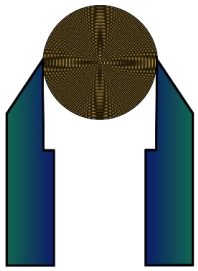

Hot Disk Sensor

Fig. 3-1 Schematic of TPS nickel bifilar sensor and kapton insulated sensor. Nano Device Laboratory, UCR

3.1.1. Theory of Hot Disk Technique

Hot Disk utilizes a bi spiral sensor element between two pieces of the sample being tested. During a transient recording the sensor is electrically heated (from 0.5 K to 5 K) and at the same time the resistance or the temperature increase of the Nickel double spiral is monitored. The heat generated in the sensor is dissipating in all directions into the surrounding two sample pieces. During a pre-set time, 200 resistance recordings are taken and from these the relation between temperature and time is established. In order to obtain a reasonably higher initial resistance of the sensor element, the Hot Disk sensor has been designed in the form of a double spiral in order to minimize the total size of the

sensor as well as to make it work with a convenient and compact configuration of the sample.

In the theoretical treatment, a hot disk sensor can be approximated as a sensor with m number of concentric rings which are equally spaced, since the sensor is designed to have uniform power density throughout the disk. Let a is the radius of largest ring, then the radius of smallest ring is a/m. Then, the total length of the heating filament is

$$L = \sum_{l-1}^{m} 2\pi l \frac{a}{m} = (m+1)\pi a \qquad [3.1]$$

Starting from the equation of heat conduction and its instantaneous point source solution, the mathematical expression of the temperature increase in the sensor surface can be obtained by integrating the point source solution over the source volume and time. During a hot disk measurement, we can only measure the temperature increase for the sensor itself. Thus, we need to determine the average temperature increase for the sensor only. This can be done by averaging the temperature rise of ring source over the length of the concentric rings. This final time dependent temperature increase [3, 4] is given by

$$\Delta T(\tau) = \frac{P_0}{\pi^{\frac{3}{2}} aK} D(\tau) \qquad [3.2]$$

Where P_0 is the total power output from the sensor, a, the radius of the sensor disk, K is the thermal conductivity of the sample that is being tested and $D(\tau)$ is a dimensionless time dependent function given by

$$D(\tau) = [m(m+1)]^{-2} \int_0^r \sigma^{-2} d\sigma \left[\sum_{i-1}^{m} l \sum_{k=1}^{m} k \; exp\left\{ \frac{-(l^2+k^2)}{4m^2\sigma^2} \right\} \; I_0 \left\{ \frac{lk}{2m^2\sigma^2} \right\} \right] \qquad [3.3]$$

Eq. 3.2 shows that the average temperature increase in the hot disk sensor is proportional to function $D(\tau)$ which is a rather complicated function of dimensionless parameter $\tau = \sqrt{kt}/a$, where k is the thermal diffusivity, a is the transient measurement time. The expression given by eq 3.2 which directly relates the temperature increase in the sensor surface to the sensor configuration, the output power, and the transport properties of the surrounding material, forms the basis of the hot disk measurement. $D(\tau)$ can be accurately evaluated to five or six significant figures if the dimensions of the sensor are known. The average temperature increase across the hot disk sensor area can be measured by monitoring the total resistance of the hot disk sensor

$$R(t) = R_0[1 + \overline{\alpha \Delta T(\tau)}] \qquad [3.4]$$

where $R(t)$ is the total resistance at time t, R_0 is the resistance of the TPS/sensor element before the transient measurement starts, α is the temperature coefficient of the resistance (TCR) of the TPS element, which is well known for nickel. Thus, this expression allows us to accurately determining $\overline{\Delta T(\tau)}$.

If the relation between t and τ is known, ΔT can be plotted as a function of $D(\tau)$, and a straight line should be obtained with slope equal to $\frac{P_0}{\pi^{\frac{3}{2}} aK}$, from which thermal conductivity, K can be calculated. Now τ depends on thermal diffusivity k, which is unknown. To calculate the thermal conductivity accurately, a series of computational plots of ΔT versus $D(\tau)$ are plotted for a range of k values, to get a final straight line once experiment is completed. This iteration process is can be done by software by

optimizing output power of the sensor and the measurement time until an optimized value of k is found. Therefore, both thermal conductivity and thermal diffusivity of the sample can be obtained by recording the single transient measurement using a hot disk sensor.

3.1.2. Experimental Setup for Hot Disk

The experiments with the hot disk are performed with the sensor sandwiched between two thin samples of equal thickness. The sensor works both as temperature sensor and heat source. The thermal conductivity equation has been solved to show the theoretical time dependence of the temperature increase; but if the transient recording is extended for a longer period for a one-dimensional sample, the temperature versus time graph becomes a straight line [5] which indicates stabilization. Such experimental conditions give values of specific heat capacity. In slab method the sensor is sandwiched between two thin circular slabs of the sample, making arrangements such that it can be assumed that the slabs are thermally insulated, so that the total input power is much more than the heat dissipation at the boundary (requirement for transient recording). This experimental method is intended for studies of the thermal conductivity and thermal diffusivity of medium- or high conducting materials (Usually with thermal conductivity greater than 10 W/mK). This method is very similar to the standard method. The two differences between the two methods are, first, the outside lateral surfaces of the sample slabs need to be insulated by a material with low thermal conductivity in order to reduce the heat losses to the surroundings. Second, heat propagates mainly in the direction of the slab plane and it is assumed that the sample is infinite in this plane. This method is also good for

ceramics, metals, silicon wafer, thin films etc. Fig. 3.2 shows the schematic of sensor-sample setup where sensor is sandwiched between two pieces of sample and acts both as heat source and thermometer.

The sample thickness t, and sensor radius a, should obey the relation $0.03 < (t/a) < 0.75$. The choice of sensor radii to match different samples is thus critical. When the transient recording begins, initially the probing depth $\Delta p < (r - a)$ where r, radius of the sample and a, radius of the sensor. The heat pulse has not yet reached the first surface of the sample; and under this condition, the thermal conductivity of the sample is evaluated. The temperature increase is expressed in terms of the characteristic time of the hot disk as in equations (3.2). When the time,

$$t \geq C_{r-a} \qquad [3.5]$$

where $C_{r-a} = (r - a)^2/K$; a constant temperature gradient is established all through the sample. In this case, $(r - a)$ is considered to be the largest distance from the sensor to the lateral sample boundary, if the geometry is non-symmetrical. The temperature increase in the sensor will then be denoted by

$$\overline{\Delta T(t)} = K + \frac{Pt}{C_{pM}} \qquad [3.6]$$

Here P is output power, M is the mass of the sample, C_p is the specific heat per unit mass. This is a linear function of t. Having known the specific heat per unit volume (ρC_p), we can calculate the thermal diffusivity, k from the equation $K = k\rho C_p$

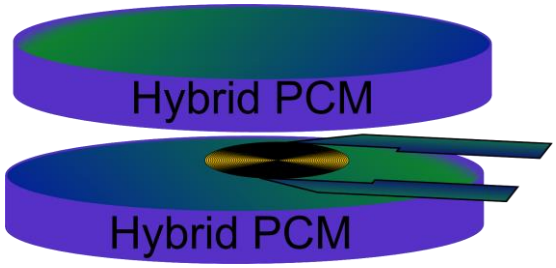

Fig. 3-2. Schematic of sensor-sample set-up in TPS hot disk technique. Reprinted with permission from P. Goli, S. Legedza, A. Dhar, R. Salgado, J. Renteria and A. A. Balandin, "Graphene-enhanced hybrid phase change materials for thermal management of Li-ion batteries", Journal of Power Sources 248 (1), 37 (2014).

3.2. Laser Flash

The Cross plane thermal conductivity was measured using a noncontact optical laser flash technique (LFT). In the LFT (NETZSCH) measurement, a xenon flash lamp produced shots with an energy of 10 J/pulse on the sample surface while the temperature rise was measured at the other end with an InSb infrared (IR) detector. The InSb IR detector is equipped with an integral dewar for liquid nitrogen cooling to keep the detector at 77 K (See Fig. 3.4). The xenon flash lamp has user selectable pulse widths (i.e. 100 µs, 400 µs, and 700 µs) to allow for accurate tuning of the transient voltage response. Here one should note the importance of sample preparation. Due to basic limitations of the experimental analysis of this LFA 447 NETZSCH instrument, certain geometries and thickness are required for the sample under test. The thermal-wave travel time allows us to measure the thermal diffusivity α. The thermal conductivity K is related to α as $K = \alpha\rho Cp$, where ρ and Cp are the mass density and specific heat of the material, respectively.

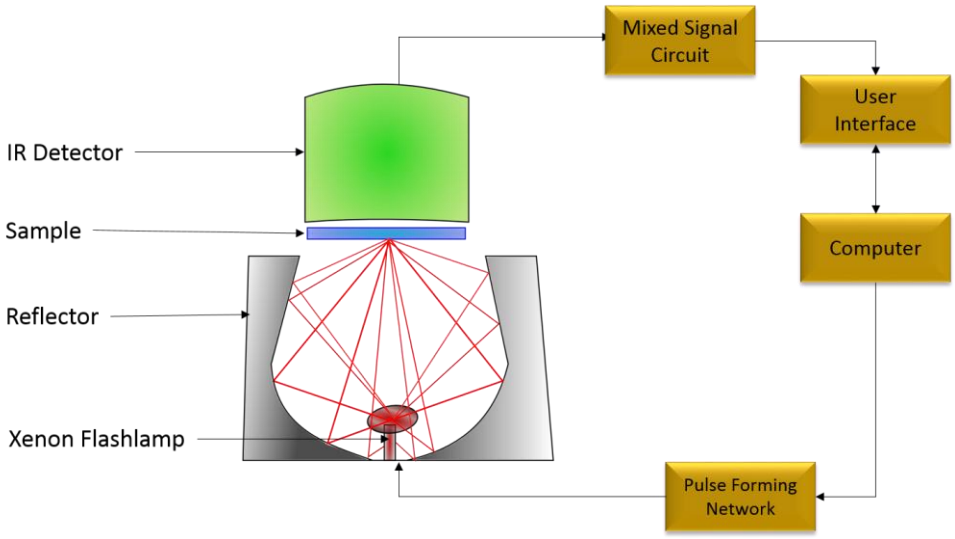

Fig. 3-3 Laser flash can be used to material thermal properties of a range of materials. The experimental setup of the laser flash includes optical stage for the sample under test, optical mask, infarred detector, mixed signal circuit, temperature control and xenon lamp and controls. It is important to note, the optical stage is custom designed when material under test do not have the specified geometry.

3.3. References

[1] S. E. Gustafsson, “Transient Plane Source Techniques for Thermal Conductivity and Thermal Diffusivity Measurements of Solid Materials”, Rev. of Sci. Instrum, 62, 3, 797–804, 1991.

[2] M. Gustavsson, E. Karawacki and S. E. Gustafsson, “Thermal Conductivity, Thermal Diffusivity, and Specific Heat of Thin Samples from Transient Measurements with Hot Disk Sensors”, Rev. of Sci. Instrum., 65, 12, 3856–3859, 1994.

[3] Y. He, “Rapid Thermal Conductivity Measurement with a Hot Disk Sensor. Part .1 Theoretical Considerations”, Thermochimica Acta, 436, 122-129, 2005.

[4] S. E. Gustafsson, K. Ahmed, A. J. Hamdani and A. Maqsood, “Transient Hot-strip Method for Measuring Thermal Conductivity and Specific Heat of Solids and Fluids: Second Order Theory and Approximations for Short Times”, J. of Appl. Phys., 53, 6064–6068, 1982.

[5] H. S. Carslaw and J. C. Jaeger, “Conduction of Heat in Solids”, United Kingdom: Oxford, 1959.

[6] S. E. Gustafsson, E. Karawacki and M. A. Chohan, “Thermal Transport Studies of Electrically Conducting Materials using the Transient Hot-strip Technique”, J. of Phys. D: Appl. Phys., 19, 727–735, 1986.

[7] J. S. Gustavsson, M. Gustavsson and S. E. Gustafsson, “On the use of the Hot Disk Thermal Constants Analyzer for Measuring the Thermal Conductivity of Thin Samples of

Electrically Insulating Materials", Proc. of the 24th Inter. Therm. Cond. Conf. Pittsburgh, PA, pp. 26-29, 1997.

[8] Instruction Manual, Hot Disk Thermal Constants Analyzer: Windows 98 Version 5.9.4, Hot Disk Inc. 2006.

[9] S. E. Gustafsson, "Hot DiskTM: Understanding the Effect of Contact Resistance," Hot Disk Application Note 10 (HDA10), 1999.

Chapter IV

PCM with Graphene Fillers

4.1. Introduction

Development[1] of Lithium-ion (Li-ion) batteries enabled progress in mobile communications, consumer electronics, automotive and aerospace industries. Li-ion batteries are an essential part of the hybrid electric vehicles (HEV) owing to their high energy densities and low weight-to-volume ratios [1]. One of the most significant factors negatively affecting Li-ion battery performance is a temperature rise beyond the normal operating range. If overheated due to short-circuiting or fast charging/discharging processes the Li-ion battery can suffer thermal runaway, cell rupture or even explosion [2]. A fire in the Li-ion battery results in the emission of dense irritating smoke which could present a serious health and environmental risk [2-3]. Combining multiple Li-ion cells close together in a battery pack in order to provide higher electric power makes the thermal management of the batteries even more challenging. The severity of the potential thermal issues with the battery packs is exemplified by a recent incident with the overheating and fire in the batteries on-board the Boeing 787 Dreamliner [4].

A common approach for thermal management of Li-ion battery packs is based on the utilization of phase-change materials (PCM). The latent heat stored in PCM, as its phase changes over a small temperature range, allows one to reduce the temperature rise inside the battery [5-7]. By varying the chemical composition of PCM one can tune its melting point and the temperature range in which it can operate as a heat absorber. It is important to note that common PCMs are characterized by very low thermal conductivity, K, with

[1] P.Goli, S. Legedza, A. Dhar, R. Salgado, J. Renteria and A. A. Balandin, "Graphene-enhanced hybrid phase change materials for thermal management of Li-ion batteries", Journal of Power Sources, 248, 37, 2014.

typical values in the range of 0.17 – 0.35 W/mK at room temperature (RT) [8]. For comparison, the RT thermal conductivity of silicon and copper are ~145 W/mK and ~381 W/mK, respectively. PCMs store heat from the batteries rather than transfer it away from the battery pack. The use of PCM in battery cells also serves the purpose of buffering the Li-ion cell from extreme fluctuations in ambient temperature. This is a different approach from what is used in the thermal management of computer chips. In order to reduce the temperature rise in a computer chip one uses thin layers of thermal interface materials (TIMs) or heat spreaders that transfer heat from the chips to heat sinks and outside packaging [9-11]. The thermal conductivity of TIMs is in the range of 1 – 25 W/mK while that of solid graphite-based heat spreaders can be on the order of 103 W/mK [12].

Here we show that these two different approaches for thermal management can be combined via introduction of the hybrid PCM with graphene acting as filler for increased thermal conductivity. Graphene is known to have extremely high intrinsic thermal conductivity [13-14] and form excellent binding with a variety of matrix materials [11, 15-16]. The graphene-enhanced hybrid PCM reveals thermal conductivity that is two orders of magnitude higher than that of conventional PCM while preserving its latent heat storage ability. Utilization of the hybrid PCM results in substantial decrease of the temperature rise inside battery packs as demonstrated under realistic conditions.

4.2. Preparation of Graphene Enhanced Composites

In order to demonstrate possible enhancement of thermal properties with graphene we selected paraffin wax (IGI-1260) as the base PCM. Paraffinic hydrocarbons, or paraffins,

are straight-chain or branching saturated organic compounds with the composition C_nH_{2n+2}. The term paraffin wax refers to mixtures of various hydrocarbon groups, particularly paraffins and cycloalkanes that are solid at ambient temperature [17]. Paraffin waxes are commonly used PCMs owing to their availability, chemical stability, and durability to cycling. Paraffin has a high latent heat of fusion (200 – 250 kJ/kg) and a range of melting points suitable for thermal control of batteries and portable electronics. The IGI-1260 paraffin wax has relatively high melting and boiling points of TM~70 ^{o}C and TB ~ 289 ^{o}C, respectively. It consists of C34-C35 hydrocarbons, which are mainly composed of n-alkanes [17]. The long hydrocarbon chains are responsible for its high density and melting point. When heated the IGI-1260 wax absorbs the heat to break the longer hydrocarbon chains into smaller ones.

The hybrid graphene-PCM composites were prepared by dispersing a solution of the liquid-phase exfoliated (LPE) graphene and few-layer graphene (FLG) in the paraffin wax at 70 ^{o}C followed by the high-shear mixing on a hot plate (Corning PC-620D) with a magnetic stirrer. The preparation temperature was selected to avoid oxidation of the paraffin wax with formation of peroxide and water. The hybrid graphene-PCM was put in molds and allowed to solidify at RT under controlled humidity conditions.

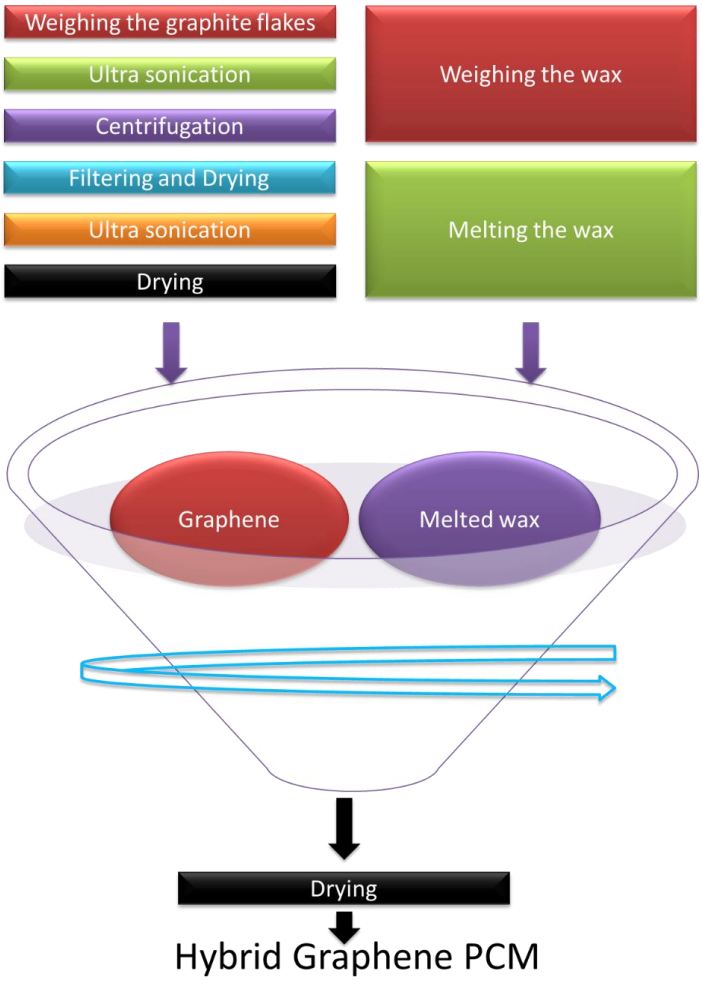

Fig. 4-1 Schematic of the grapheme-enhanced preparation

Three types of LPE graphene were used for the filler. For low loading fractions up to 1%, we used graphene solution with the average thickness of one monolayer (0.35 nm) and the lateral size distribution in the range from 150 to 3000 nm with 550 nm average size. We refer to this material, which is predominantly single-layer graphene, as graphene

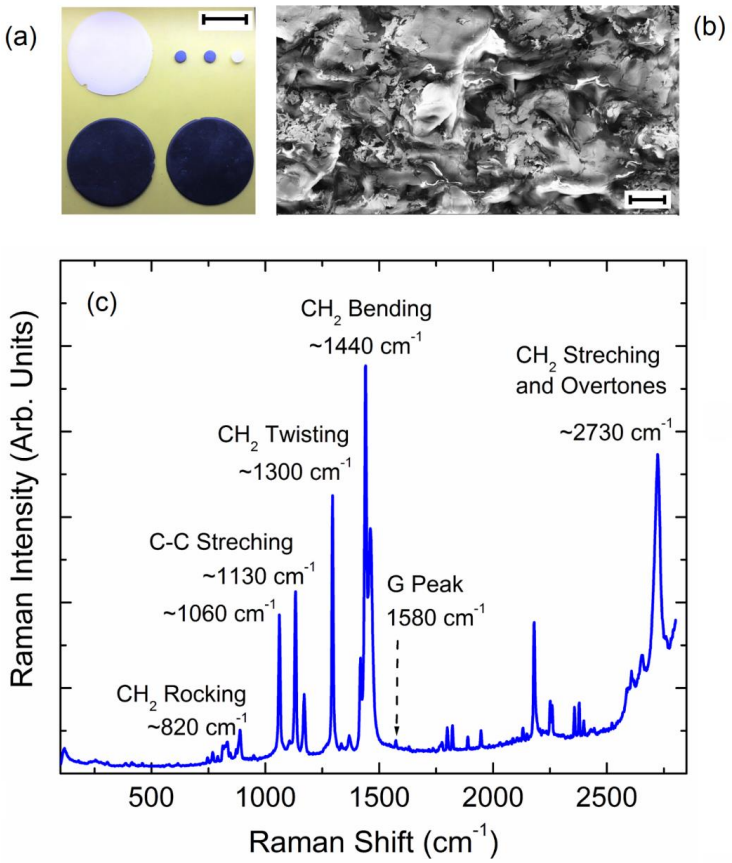

filler type

Fig. 4-2 Hybrid graphene – paraffin phase change material. (a) Optical image of the PCM samples showing the change in color with increasing graphene content. (b) Scanning electron microscopy image of the hybrid graphene-PCM indicating uniform distribution of the graphene flakes. (c) Raman spectrum of the graphene-paraffin composite. The main bands are indicated in the legends. The graphene G peak is weak compared to hydrocarbon signatures due to its small concentration and smaller scattering cross-section.

A. For high loading fractions up to 20 %, we used two other types of FLG. The graphene filler type B had an average FLG flake thickness of ~ 1 nm, which constitutes about 3

atomic planes with an average lateral dimension of ~10 μm. The graphene filler type C had an average flake thickness of 8 nm, which constitutes 20-30 atomic planes with a lateral size in the range of 150 and 3000 nm with ~550 nm average. Fig 4.2 (a) shows an optical image of the resulting molded disks of the hybrid graphene-PCM composite with the graphene-FLG loading fraction varying from 0.5 to 20 wt. %. The color of the disks changes from white to black as the fraction of graphene increases. It was observed that the addition of graphene leads to some reduction of TM. The dispersion of graphene – FLG in the paraffin matrix was checked with the scanning electron microscopy (SEM) (see Fig. 4.2 (b)). It was confirmed that graphene – FLG fillers were evenly distributed throughout the sample. We did not observe differences between the surface and the interior of the composite samples.

The incorporation of graphene into paraffin matrix was monitored using micro-Raman spectroscopy (Renishaw In-Via). The vibrational spectra of paraffin are known to have a large number of informative bands that show variations with the change in paraffin's state and composition [18-22]. The measurements were performed in the backscattering configuration under $\lambda = 488$ nm laser excitation. Fig. 4.2 (c) shows Raman spectrum of the hybrid graphene – paraffin wax. The clearly identified vibrational bands are CH2 rocking at ~650 – 850 cm^{-1}, C-C skeletal stretching at 1060 cm^{-1} (symmetric) and 1130 cm^{-1} (asymmetric), CH_2 twisting at 1300 cm^{-1}, CH_2 bending at 1440 cm^{-1}, and overtones of bending vibrations at above ~2000 cm^{-1}. A small peak at 1580 cm^{-1} was identified as graphene's signature G peak. Its intensity is much lower than that of long hydrocarbon chains of paraffin. Graphene's incorporation into paraffin resulted in changes of some

paraffin peaks and the appearance of new features in the spectra suggesting modification of the vibrational modes due to the attachment of graphene flakes to the long hydrocarbon chains. The observed changes were shifts of some of the main paraffin Raman peaks by 1-4 cm^{-1} after addition of graphene. Although it is difficult to quantitatively describe the changes, the detailed calibration of Raman spectra with the amount of graphene loading and sample preparation conditions allowed us to achieve a consistent composition of the hybrid graphene-PCM.

4.3. XPS and Raman Spectra of Graphene-Enhanced Phase Change Material

The changes with the hydrocarbon chains and increasing concentration of SP^2-bonded carbon have also been confirmed with X-ray photoelectron spectroscopy (XPS) analysis (Kratos AXIS ULTRADLD). The XPS data provides quantitative information on the elemental composition, empirical formula and chemical state of the composite. Fig. 4.3 (a) shows XPS survey scans of IGI-1260 pristine parffin wax. The XPS results show the presence of hydrocarbon with 284.9 eV energy. The C1s spectrum of IGI-1260 is characeterized by the transition centered at 284.9 eV, which corresponds to H-C and C-C bonds. The C1s line intensity changes with addition of graphene to the hybrid graphene – PCM composite. Fig. 4.3 (b) presents the counts per second of hydrocarbon as a function of graphene concentration in the composites. One can see from XPS spectra that the SP^1 hydrocarbon quantity decreased with increasing of amount of graphene in the paraffin wax. The reduction of number H-C chains in the hybrid composites suggests that

graphene is reacting with alkane chains of paraffin in the hybrid graphene – PCM composite.

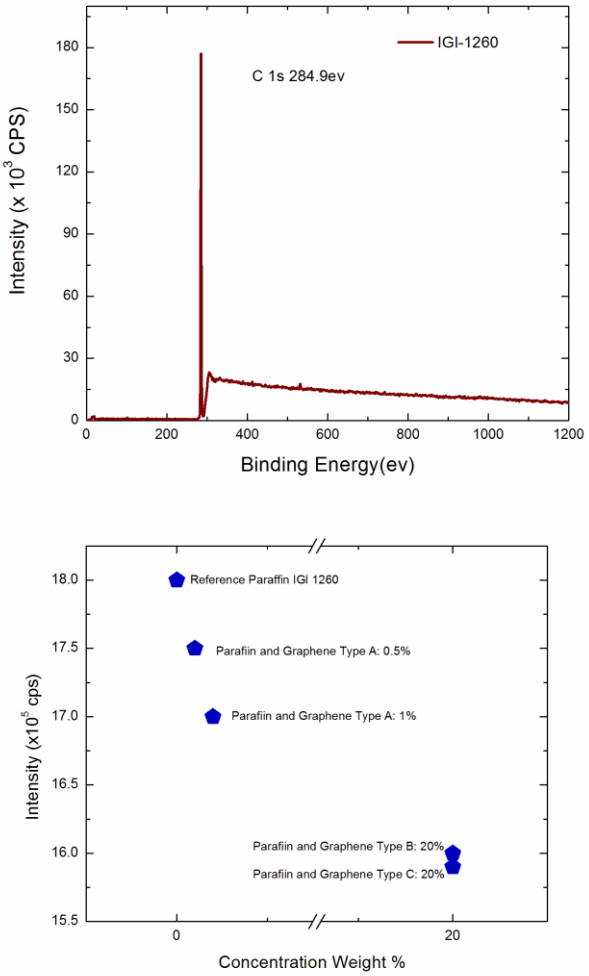

Fig. 4-3(a) XPS data for pristine paraffin IGI-1260 showing presence of hydrocarbons with characteristic transition energy of 284.9 eV. (b) Counts per second of hydrocarbon as a function of graphene loading.

4.4. Thermal Conductivity of Graphene-Enhanced Phase Change Materials

The thermal conductivity of the graphene – paraffin samples was measured using the transient planar source (TPS) technique (Hot Disk TPS2500). The results of the measurements are the drift and transient graphs. Depending on the sample size and thickness different modes of the data extraction are used. They include the (i) standard method for bulk materials, (ii) slab method for thin material (from 0.5 mm to 5 mm) and

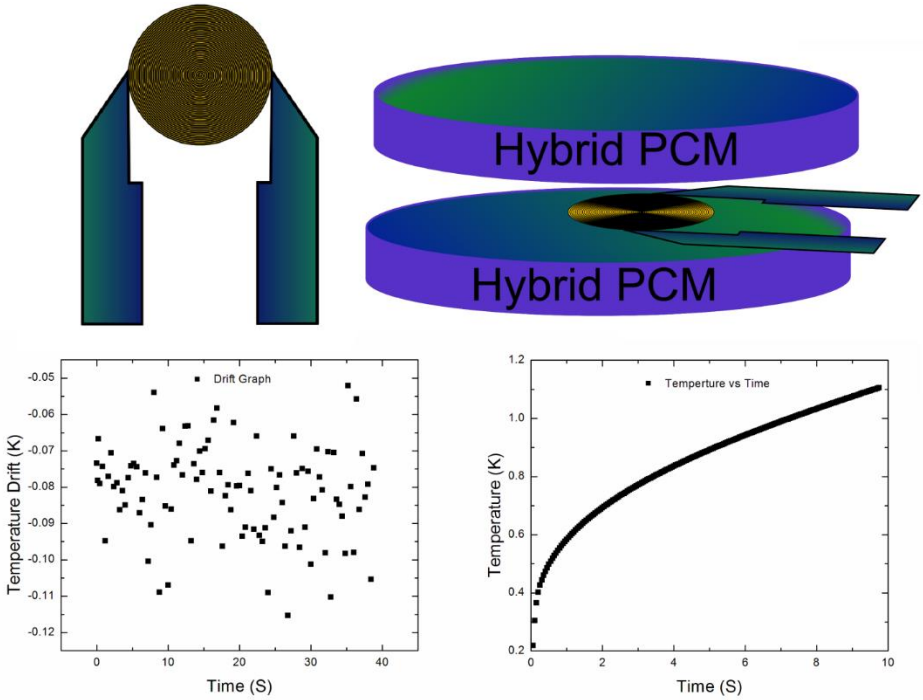

Fig. 4-4 Illustration of the thermal conductivity measurement. (a) Hot disk sensor, which is used as a heat source and as a dynamic temperature sensor. (b) Sensor is sandwiched between two identical pieces of a sample under test. (c) The drift graph represents the measured sensor temperature increase before the sample heating. The uniform data point scatter indicates that the isothermal conditions are satisfied. (d) Experimental transient response of the sample temperature to the heat pulse used for the thermal data extraction.

(iii) think-film method for films of thickness from 10 to 500 microns. The drift graph represents the measured sensor temperature increase before heating the sample (40 seconds of measurements and 101 data points). For a successful measurement, the graph has to be uniform scatter of data points, relatively flat or horizontal, representative of isothermal conditions for the sample prior to the measurement. If the sample was not

isothermally stable an upward or downward trend in the graph is observed. The transient graph displays

the temperature increase of the sensor during the heating of the sample (200 data points in total). Fig.4.4 shows an example of the experimental raw data indicating that the isothermal conditions were met and the measurement procedures were adequate for the samples under study.

Fig. 4.5 (a) presents the measured thermal conductivity of the pristine paraffin wax IGI-1260 and hybrid PCM composites with different graphene- FLG loading. More than ten samples were investigated for each loading fraction to ensure reproducibility. The measured thermal conductivity for the pristine paraffin was K=0.25 W/mK, which is in agreement with the literature values. One can see a drastic increase of K in the composites with the addition of graphene-FLG filler. The thermal conductivity of the hybrid graphene-PCM reaches ~15 W/mK at RT with the small 1 wt. % loading fraction. This is a significant increase by a factor of 60. The highest value achieved at 20 wt. % loading was ~45 W/mK, which is more than a *two order magnitude* of enhancement.

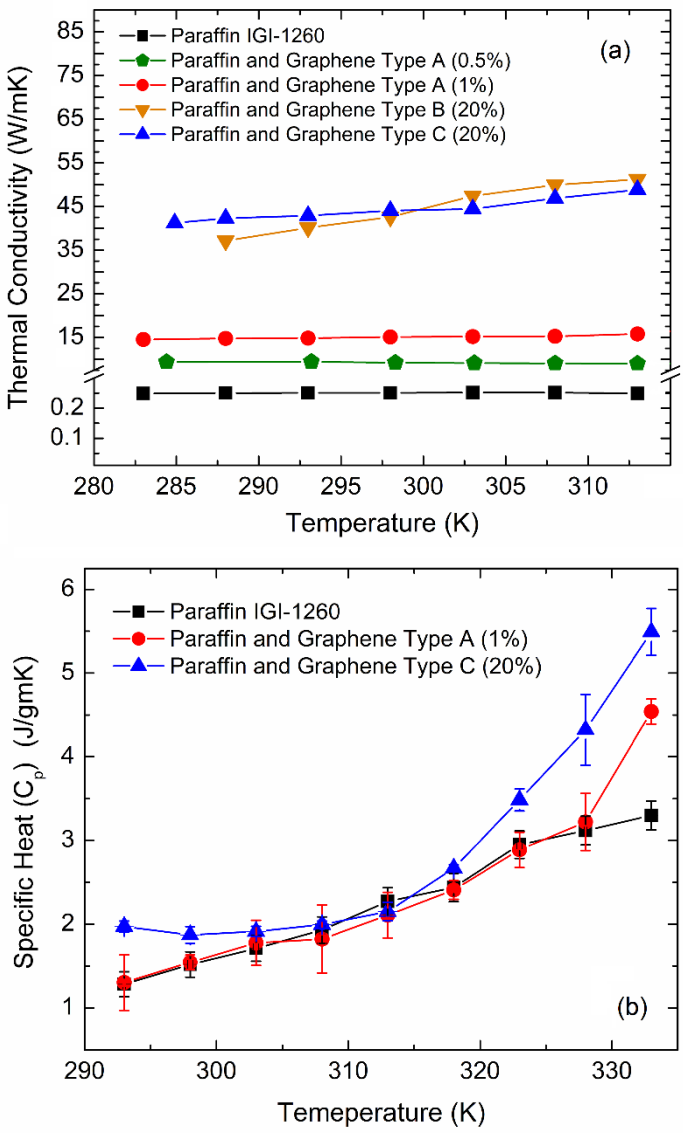

Fig. 4-5 (a) Thermal conductivity of the graphene – paraffin composites with different graphene loading as the function of temperature. The results for pristine paraffin (IGI-1260) are also shown for comparison. (b) Specific heat of the composites and reference pristine paraffin as the function of temperature.

The thermal conductivity enhancement factor, Ɛ=(K-Km)/Km, of about 60 at the 1 wt. % loading fraction is exceptionally high compared with the values reported for either PCMs with fillers [28-30] or TIMs [11, 15-16] (K is the measured thermal conductivity of the composite and Km is the thermal conductivity of the paraffin matrix). There are two

possible reasons for substantial increase of the thermal conductivity of composites: formation of a thermally percolating network of graphene flakes or strong binding of the graphene flakes to paraffin matrix. The percolation threshold in thermal composites was mostly discussed in the context of carbon nanotubes, carbon fibers or other fillers with cylindrical geometry and high aspect ratio [31-34]. The results obtained for cylindrical high-aspect ratio fillers cannot be readily extended to graphene and FLG fillers. The physics of thermal percolation is also a subject of debates [10, 31-33]. Unlike electrical percolation, the thermal percolation threshold can be less pronounced due to heat conduction by the matrix. Based on the fact that the electrical conductivity of the samples has not changed after addition of graphene and prior work on graphene fillers in thermal interface materials [11, 16], it is reasonable to assume that evenly dispersed graphene flakes with a lateral size in the range from 150 to 3000 nm are unlikely to form a percolating network at 1 wt. % by themselves.

The strong increase of the thermal conductivity of the composite can be explained by good attachment of hydrocarbon molecules to graphene flakes at the experimentally determined processing temperature. The C_nH_{2n+2} – graphene attachment reduces the thermal interface resistance between the matrix material and filler. Modification of some of the Raman signatures of paraffin after addition of graphene is consistent with this assertion. It was reported [13, 16] that graphene has a much lower thermal Kapitza resistance, $RB=\Delta T/(Q/A)$, with many matrix materials as compared to carbon nanotubes (here ΔT is temperature differences between two materials forming an interface, Q is the heat flux and A is the surface area). The attachment does not necessarily need to be

covalent bonding to improve heat conduction from fillers to matrix [34]. More studies are required in order to completely clarify the nature of bonding in such graphene – paraffin systems.

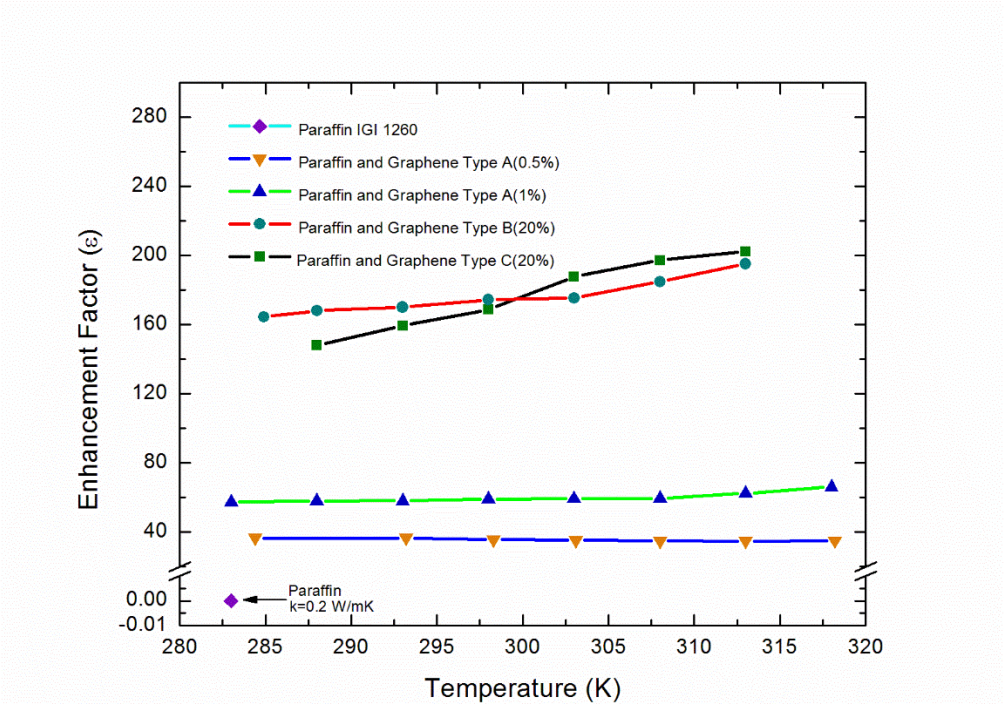

Fig. 4-6 Enhancement factor as a function of Temperature

In the case of paraffin and graphene the thermal coupling between the matrix and filler is likely even stronger than in other matrix-filler combinations. The *ab initio* density function theory calculations and molecular dynamics simulations suggested the possibility of extraordinary enhancement of thermal conductivity in ordered graphene composites with organic matrix where the heat transport is along the direction of the graphene planes: $K/K_m \approx 360$ at graphene loading of 5% [35]. The thermal conductivity in the direction perpendicular to the graphene planes almost does not change, according to the same study [35]. The strong anisotropic increase in the heat conduction was attributed

to graphene's planar geometry and strong coupling to the octane molecules resulting in the corresponding decrease in the Kapitza resistance [36-38]. This means that heat carrying phonon modes excited in graphene can couple well to those in organic molecules. Although a direct quantitative comparison between our graphene-paraffin composite and the composite studied in Ref. [35] is not possible one can conclude that even randomly oriented graphene flakes should produce significant increase in the thermal conductivity of composites in agreement with our experiments.

Thermal conductivity of all composites revealed only weak temperature dependence, which is beneficial for PCM practical applications. This weak dependence is expected for disordered materials. Improvement in the thermal management applications of the hybrid graphene-PCM can only be achieved if the increase in the thermal conductivity is achieved without degradation of the latent and sensible heat storage capacity. Possible changes in T_M due to graphene loading should also be adjusted. We performed the specific heat, C_p, measurements (NETZSCH) with a set of the samples with the thicknesses of 1 mm − 1.6 mm to ensure that their thermal resistances were much larger than the contact thermal resistances. As a control experiment we measured specific heat of pristine paraffin wax. Fig. 4.5 (b) presents the specific heat data in the examined temperature range. The specific heat for the reference paraffin wax is ~2 kJ/kgK at RT, which is consistent with literature values. Near RT, the specific heat does not change much with the addition of graphene filler. The difference appears in the higher temperature range. The hybrid graphene-PCM has larger specific heat than the reference paraffin. The growth of C_p at the temperature increases above 320 – 330 K is expected.

In paraffins, the specific heat starts to increase as temperature approaches T_M and then falls off again [17].

4.5. Thermal Management of Battery Packs with Graphene Phase Change Materials

In order to directly prove that the developed hybrid graphene-PCM composites can significantly improve the thermal management of Li-ion batteries we performed the battery testing under realistic conditions. Fig. 4.7 shows the experimental setup for the battery testing. We used six 4-V Li-ion cells with the capacity of 3000 mAh each placed in a standard aluminum battery pack. The measurements were performed with the charger-discharger setup (HYPERION EOS 720i) and the temperature probes (Applent AT4516) that logged temperature for the assigned time intervals. The first two temperature probes were placed inside the battery pack, the third probe was connected to the battery pack shell acting as the heat sink and the fourth probe was used to collect the ambient temperature data. During the measurements the batteries were charging-discharging at 16 A and 5 A, respectively. The first control experiment was performed with pristine paraffin wax, which was melted and poured into the aluminum cylinder containing Li-ion battery cells. Special care was taken to ensure that the wax completely filled the space between the cylinders as in conventional battery designs. The battery pack with paraffin was allowed to cool to RT and then tested through ten charge/discharge cycles. The experiments with the hybrid graphene-PCM followed the same protocol.

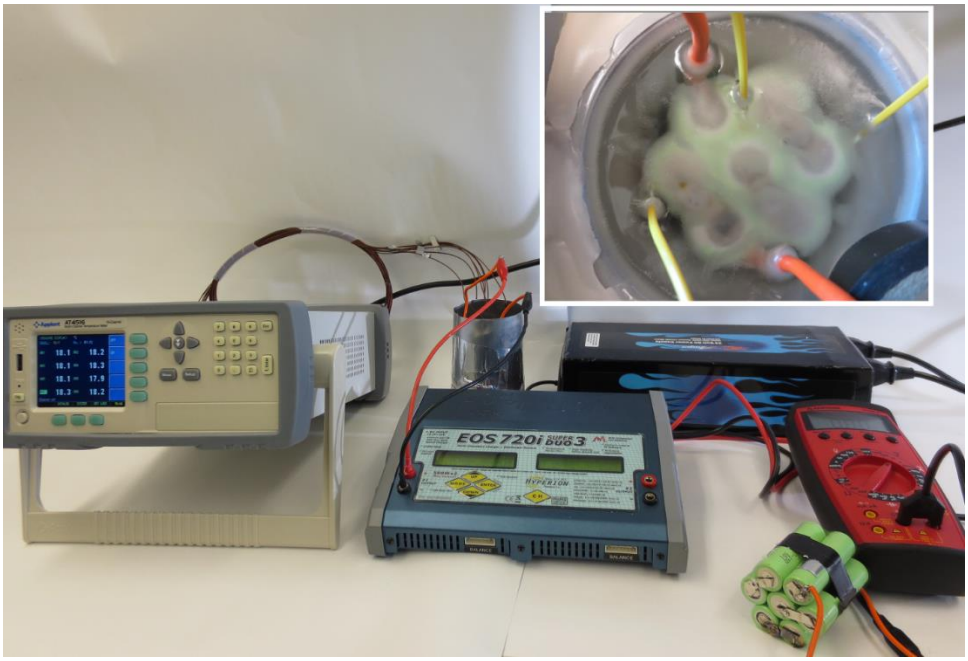

Fig. 4-7 The experimental setup included six 4-V Li-ion cells with the capacity of 3000 mAh each, which were placed in a standard aluminum battery pack

Fig. 4.8 shows temperature as a function of time during the charging-discharging cycles for the Li-ion battery pack with IGI-1260 as PCM. One can see that the temperatures of the anode and cathode are higher than that of the outside shell (indicated in the figure as the battery pack temperature). The variation of the ambient T during the measurement explains some background variation in the temperature cycles. The results of the tests of the hybrid graphene-PCM are summarized in Fig. 4.9. One can see that when no PCM was used in the battery pack (the heat dissipates through the air and metal bottom of the pack) the temperature rise inside the battery (sensor attached to anode/cathode) is the highest: $\Delta T \sim 37\ ^{o}C$. The use of conventional PCM results in the decrease of the temperature rise to ~24 ^{o}C. The Li-ion battery pack with the developed hybrid graphene-PCM reveals the lowest temperature rise of ~10 ^{o}C during the first cycle. The temperature rise increases to ~16 ^{o}C after the third cycle and saturates at this value. The

temperature rise for the case of the hybrid graphene-PCM with the larger loading fraction saturates at ~ 13 ^{o}C. One should note here that the outside shell (battery pack) made of thin aluminum was not an optimized heat sink. Attachment of the outside shell to a good heat sink would make the improvement in thermal management with the hybrid graphene PCM even more pronounced.

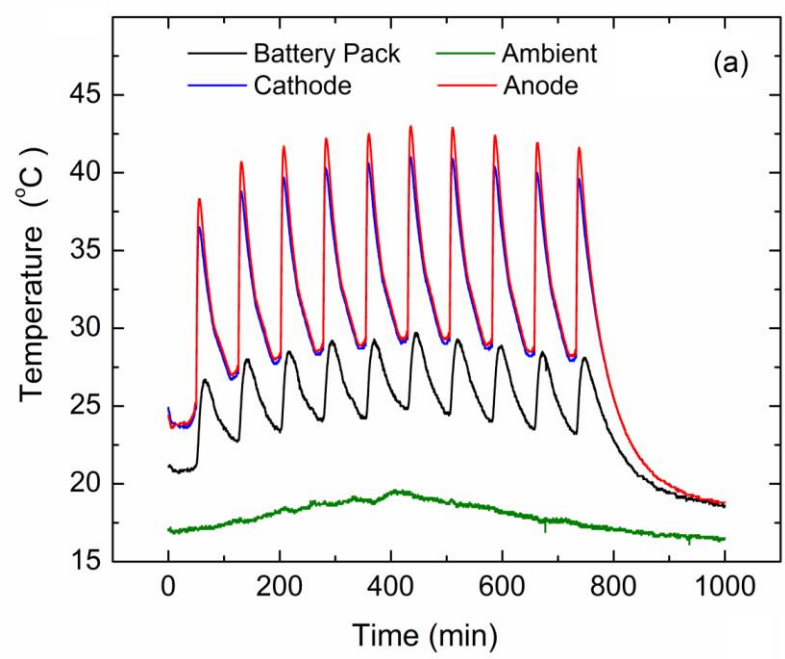

Fig. 4-8 Measured temperature fluctuations inside and outside the battery pack with reference paraffin used as the phase change material. The temperatures are recorded at the battery cylinder cathode (blue), battery cylinder anode (red) and battery pack shell (black). The ambient temperature charge during the measurement is also shown (green).

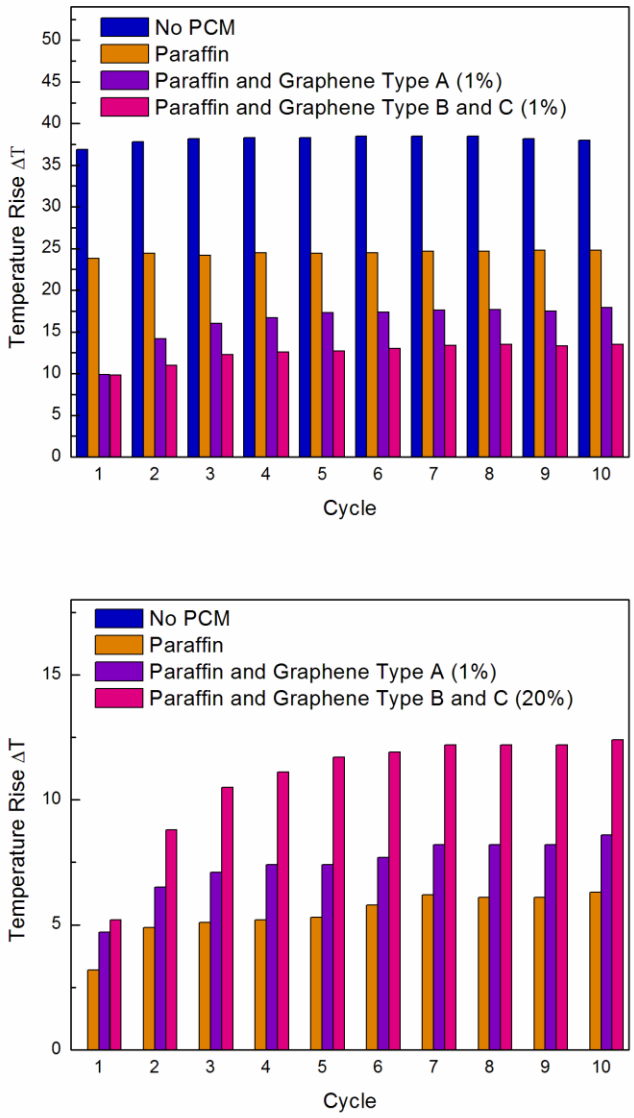

Fig. 4-9 Diagram of the temperature rise inside the Li-ion battery pack during the first ten charging – discharging cycles for the battery pack without PCM (red), with conventional paraffin PCM (blue), with the hybrid graphene-PCM at 1 wt. % loading (orange) and with the hybrid graphene-PCM at 20 wt. % loading (green). Note that the developed hybrid graphene-PCM strongly reduces the temperature rise inside the battery by simultaneously absorbing the heat and conducting it to the outside shell. The reduction in the temperature rise can be made stronger with a proper design of the outside heat sink.

The dependence of ΔT on the number of cycles, observed in Fig. 4.9, reflects the physical mechanisms behind the cooling action of conventional PCM and the hybrid graphene-PCM. The conventional PCM mostly absorbs the heat from the battery cylinders conducting only its small portion to the battery pack shell. The hybrid graphene-PCM stores and conducts heat simultaneously. This results in lower ΔT inside the battery pack but also increases the temperature of the outside shell. The increasing temperature of the shell results in some increase in ΔT inside the battery as well. In order to elucidate this difference in cooling action, in our experiments we intentionally did not connect the outside shell, which constitute the battery pack, to any specially designed heat sink. In practical automotive and aerospace applications one can readily envision a proper thermal connection of the battery packs to the heat sinks, e.g. to the heavy vehicle frame in HEVs. The latter will eliminate or reduce ΔT of the outside shell further improving thermal management with the hybrid graphene-PCM.

4.6. Numerical Modeling Approach

The modeling of the conductive heat flow in the Li-ion battery pack was performed using COMSOL software package (Multiphysics and Heat Transfer Module). A three-dimensional (3D) model was constructed to simulate and analyze six cylindrical Li-ion batteries in the pack filled with different medium. The geometric characteristics include six Li-ion batteries with 18.4 mm diameter evenly distributed within a solid cylinder with 70 mm diameter, which represent an aluminum sheath of 1 mm in thickness. Owing to the simple geometry of the battery pack, we used a coarse mesh of free tetrahedrals for

the aluminum sheath, the solid cylinders, and the heat conduction medium in which these cylinders were encased. The free tetrahedrals were evenly scaled in all directions and the complete mesh consisted of 11796 such elements. The transient conductive heat transfer in solids is defined by the equation $C_p(\partial T/\partial t) = \nabla \cdot (K\nabla \mathrm{T}) + Q$, where ρ is the mass density (kg/m^3), C_p is the specific heat capacity at constant pressure (J/kgK), T is the absolute temperature (K), K is the thermal conductivity (W/mK), Q is the power density (W/m^3) and t is time. In all simulation runs we modified only the material characteristics of the medium that fills the space among the battery cylinders. These characteristics included the values for the air and paraffin phase change material. For example, for paraffin wax without graphene we used the thermal conductivity K = 0.25 W/mK, mass density, ρ = 900 kg/m^3, and heat capacity, C_p = 2500 J/kgK. The simulation results included the transient data, e.g. plots of temperature vs. time for specific locations inside battery packs, and temperature distributions inside the battery packs at any given moment. The simulation results were compared with the empirical data collected for the battery packs.

Computer simulation of the passive PCM thermal management systems for Li-ion battery packs is known to give valuable information for materials and system optimization [40-41]. We further analyzed our experimental results via numerical solution of the heat diffusion equation for the specific battery design and measured specific heat and thermal conductivity. The details of the model and simulation procedures are provided in the Methods section. Fig. 4.10 shows the schematic of the Li-ion battery pack and the simulated temperature profiles for the four cases, which corresponded to the conducted

experiments. In the case of no PCM between the battery cylinders and the outside shell, the temperature in the cylinders is at its maximum of above 330 K. The outer shell also heats up to ~315 K via conduction through the air. The use of the standard paraffin wax reduces the temperature of the cylinders to around 320 K without heating the outside shell. Thermal management with hybrid graphene PCM results in the lowest temperature of the battery cylinders of ~310 – 315 K with some increase in the temperature of the outside shell. The temperature profile is much more uniform when the hybrid graphene PCM is used. One should note here again that connecting the outside shell to a proper heat sink would improve the performance of the hybrid PCM further.

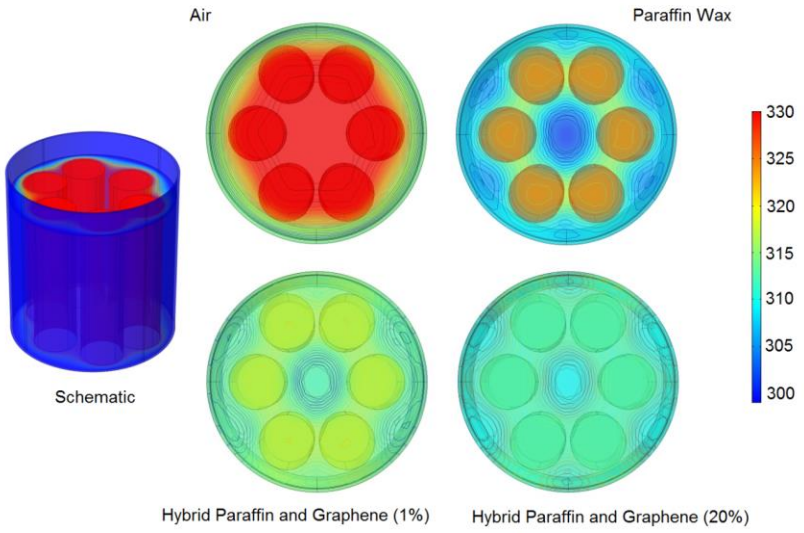

Fig. 4-10 Simulated temperature profiles in Li-ion battery packs obtained using the measured values of the specific heat and thermal conductivity. The simulation data are in agreement with the experiments.

We demonstrated that the use of graphene and few-layer graphene as fillers in organic phase change material allows one to increase its thermal conductivity by more than two orders of magnitude while preserving its latent heat storage ability. The strong

enhancement is achieved via easy binding of graphene flakes to paraffinic hydrocarbons resulting in good thermal coupling. The exceptionally large thermal conductivity of graphene improves the heat conduction ability of paraffins. It was also shown through measurements and computer simulations that improved thermal properties of graphene PCM result in significant temperature rise inside realistic Li-ion battery packs. The described combined heat storage – heat conduction approach may lead to a transformative change in thermal management of batteries.

4.7. References

[1] D. Linden and B. T. Reddy, "Handbook of Batteries", McGraw-Hill, New York, 2002.

[2] R. Spotnitz and J. Franklin, "Abuse behavior of high-power, lithium-ion cells", Journal of Power Sources (Elsevier), 113, 81–100, 2003.

[3] C. Mikolajczak, M. Kahn, K. White and T. R. Long, "Lithium-Ion Batteries Hazard and Use Assessment" Fire Protection Research Foundation, 76, 90, 102, 2011.

[4] FAA Press Release. (2013) Federal Aviation Administration. January 16.

[5] B. Zalba, J. M. Marin and L. F. Cabeza, "Review on thermal energy storage with phase change: materials, heat transfer analysis and applications", Applied Thermal Engineering, 23, 3, 251, 2003.

[6] F. Agyenim, N. Hewitt, P. Eames and S. Mervyn, "A review of materials, heat transfer and phase change problem formulation for latent heat thermal energy storage systems (LHTESS)", Renewable and Sustainable Energy Review, 14, 615, 2010.

[7] M. M. Farid, A. M. Khudhair, S. A. Razack and S. Al-Hallaj, "A review on phase change energy storage: materials and applications" Energy Conversion and Management 45, 1597, 2004.

[8] S. D. Sharma and K. Sagara, “Latent heat storage materials and systems: A Reveiew” J. Green Energy, 2, 1, 2005.

[9] S. V. Garimella, A. S. Fleischer, J. Y. Murthy, A. Keshavarzi, R. Prasher, C. Patel, S. H. Bhavnani, R. Venkatasubramanian, R. Mahajan, Y. Joshi, B. Sammakia, B. A. Myers, L. Chorosinski, M. Baelmans, P. Sathyamurthy and P. E. Raad, “Thermal Challenges in Next-Generation Electronic Systems”, IEEE Trans. Compon. Packag. Technol., 31, 801−815, 2008.

[10] R. Prasher, “Thermal conductivity of composites of aligned nanoscale and microscale wires and pores”, Proc. IEEE 94, 1571−1585, 2006.

[11] K. M. F. Shahil and A. A. Balandin, “Graphene - multilayer graphene nanocomposites as highly efficient thermal interface materials”, Nano Letters, 12, 861, 2012.

[12] A. Yan, G. Liu, J. M. Khan and A. A. Balandin, “Graphene quilts for thermal management of high-power GaN transistors”, Nature Communications 3, 827 2012.

[13] A. A. Balandin, “Thermal properties of graphene and nanostructured carbon materials”, Nature Materials, 10, 569 – 581, 2011.

[14] D. L. Nika and A. A. Balandin, “Two-dimensional phonon transport in graphene”, Journal of Physics: Condensed Matter, 24, 233203, 2012 .

[15] V. Goyal and A. A. Balandin, “Thermal properties of the hybrid graphene-metal nano-micro-composites: Applications in thermal interface materials”, Applied Physics Letters, 100, 073113, 2012.

[16] K. M. F. Shahil and A. A. Balandin, “Thermal properties of graphene and multilayer graphene: Applications in thermal interface materials” Solid State Communications 152 , 1331, 2012.

[17] M. Freund, R. Csikos, S. Keszthelyi and G. Y. Mozes, “Paraffin Products properties, technologies, applications”, Elseiver, 14, 1981.

[18] J. K. Brown, N. Sheppard and D. M. Simpson, “The Interpretation of the Infra-Red and Raman Spectra of the n-Paraffins” Math. Phys. Sci. 247, 35, 1954.

[19] H. G. M. Edwards and M. J. P. Falk, “Fourier-transform Raman spectroscopic study of unsaturated and saturated waxes”, Spectrochim. Acta Part A, 53, 2685, 1997.

[20] K. Kalyanasundaram and J. K. Thomas, “The conformational state of surfactants in the solid state and in micellar form. A laser-excited Raman scattering study”, J. Phys. Chem 80, 1462, 1976.

[21] R. A. MacPhail, H. L. Strauss and R. G. Snyder, “Carbon-hydrogen stretching modes and the structure of n-alkyl chains. 2. Long, all-trans chains”, J. Phys. Chem. 88, 334, 1984.

[22] M. Zheng and W. Du, “Phase behavior, conformations, thermodynamic properties, and molecular motion of multicomponent paraffin waxes: A Raman spectroscopy study”, Vibrational Spectroscopy, 40, 219, 2006.

[23] S. E. Gustafsson, “Transient plane source techniques for thermal conductivity and thermal diffusivity measurements of solid materials”, Rev. Sci. Instrum. 62(3), 797, 2006.

[24] L. Xia, P. Zhang, and R. Z. Wang, “Preparation and thermal characterization of expanded graphite/paraffin composite phase change material”, Carbon, 48, 2538, 2010.

[25] Y. He, “Rapid thermal conductivity measurement with a hot disk sensor: Part 1. Theoretical considerations, Part 2. Characterization of thermal greases”, Thermochim. Acta, 436, 130,122, 2005.

[26] S. Ghosh, D. Teweldebrhan, J. R. Morales, J. E. Garay and A. A. Balandin, “Thermal properties of the optically transparent pore-free nanostructured yttria-stabilized zirconia”, J. Appl. Phys., 106, 113507, 2009.

[27] M. Shamsa, S. Ghosh, I. Calizo, V. Ralchenko, A. Popovich and A. A. Balandin, “Thermal conductivity of nitrogeneated ultrananocrystalline diamond films on silicon”,. J. Applied Physics, 103, 083538, 2008.

[28] K. Chintakrida, R. D. Weinstein and A. S. Fleischer, “A direct comparison of three different material enhancement methods on the transient thermal response of paraffin phase change material exposed to high heat fluxes”, Int. J. Thermal Sciences, 50, 1639, 2011.

[29] R. Ehid, R. D. Weinstein and A. S. Fleischer, “The shape stabilization of paraffin phase change material to reduce graphite nanofiber settling during the phase change process”, Energy Conversion and Management, 57, 60, 2012.

[30] J. Wang, H. Xie, Z. Xin, Y. Li and L. Chen, “Enhancing thermal conductivity of palmitic acid based phase change materials with carbon nanotubes as fillers” Solar Energy 84, 339, 2010.

[31] L. Berhan, L and A. M. Sastry, “Modeling percolation in high-aspect-ratio fiber systems. II. The effect of waviness on the percolation onset” Phys. Rev. E, 75, 041121, 2007.

[32] S. U. S. Choi, Z. G. Zhang, W. Yu, F. E. Lockwood, and E. A. Grulke, “Anomalous thermal conductivity enhancement in nanotube suspensions” Appl. Phys. Lett., 79, 2252 2001.

[33] N. Shenogina, S. Shenogin, L. Xue, P. Keblinski, “On the lack of thermal percolation in carbon nanotube composites”, Appl. Phys. Lett., 87, 133106, 2005.

[34] R. Gulotty, M. Castellino, P. Jagdale, A. Tagliaferro and A. A. Balandin, “Effects of Functionalization on Thermal Properties of Single-Wall and Multi-Wall Carbon Nanotube–Polymer Nanocomposites”, ACS Nano 7, 5114, 2013.

[35] D. Konatham, K. N. D. Bui, D. V. Papavassiliou and A. Striolo, “Simulation insights into thermally conductive graphene-based nanocomposites”, Mol. Phys., 109, 97−111, 2011.

[36] D. Konatham and A. Striolo, “Thermal boundary resistance at the graphene-oil interface”, Appl. Phys. Lett., 95, 163105, 2009.

[37] D. Konathan D. V. Papavassiliou and A. Striolo, “Thermal boundary resistance at the graphene–graphene interface estimated by molecular dynamics simulations” Chem Phys Lett. 527, 47, 2012.

[38] S. E. Gustafsson, E. Karawacki and M. A. Chohan, “Thermal transport studies of electrically conducting materials using the transient hot-strip technique”, J. Phys. D 19, 727, 1986.

[39] M. Gustavsson, H. Wang, R. M. Trejo, E. Lara-Curzio, R. B. Dinwiddie and S. E. Gustafsson, “On the Use of the Transient Hot-Strip Method for Measuring the Thermal Conductivity of High-Conducting Thin Bars”, Int. J. Thermophys., 27, 1816, 2006.

[40] A. Mills, S. Al-Hallaj, “Simulation of passive thermal management system for lithium-ion battery packs”, J. Power Sources, 141, 307, 2005.

[41] R. Kizilel, R. Sabbah, J. R. Selman and S. Al-Hallaj, “An alternative cooling system to enhance the safety of Li-ion battery packs”, J. Power Sources, 194, 1105, 2009.

Chapter V

CNT as Part of Electrode Design

5.1. Introduction

We report[2] the results of investigation of thermal properties of a set of different Li-ion battery electrodes enhanced with multi-wall carbon nanotubes. The electrodes were synthesized via an inexpensive scalable filtration method, which can be extended to commercial electrode-active materials. The best performing electrodes contained a layer of γ-Fe_2O_3 nanoparticles on carbon nanotubes sandwiched between two layers of carbon nanotubes. Our "hot disk" and "laser flash" measurements reveal that the in-plane (cross-plane) thermal conductivity of the cathodes with the highest battery capacity was ~50 W/mK (3 W/mK) at room temperature. These values are up to two-orders-of-magnitude higher than those for conventional electrodes based on carbon black. The highest in-plane thermal conductivity achieved in the carbon-nanotube-enhanced electrodes was ~141 W/mK. The obtained results are important for thermal management of Li-ion and other high-power-density batteries.

Owing to their superior power-density Li+-ion batteries are used in a wide variety of applications [1]. At the same time, this and similar types of batteries have a serious drawback, which is overheating and related safety concerns [2]. The heat is generated during the operation of any battery as current flows through the internal resistance of the battery whether it is being charged or discharged [2-3]. In the case of discharging, the temperature rise is limited by the available energy. No such limit exists in the charging cycle when energy can be pumped even after full charging of the battery [3]. In addition

[2] Partially reprinted from P. Goli, B. Koo, A. Sumant, C. D. S. Carlo, T. Rajh, C. Johnson, A. A. Balandin and E. V. Shevchenko, "Carbon-Nanotube Enhanced Li-Ion Battery Electrodes with Signiffcantly Increased Thermal Conductivity", Manuscript under preperation

to Ohmic heating, chemical reactions that take place during charging and discharging in Li+-ion batteries can also contribute to overheating. If overheating of the battery is not properly addressed, thermal runaway may cause a catastrophic destruction of the battery. From the other side, efficient heat removal from the battery allows for higher electrical currents to be achieved resulting in faster charging rates. These considerations explain the importance of thermal management for operation and safety of any kind of high-power batteries.

There are a number of commonly used methods for removal of the excessive heat from the batteries, e.g. increasing the air flow around the battery or maximizing the surface area of the electrodes [4]. However, implementation of sophisticated engineered control methods for active cooling via enhanced air flow significantly increases the complexity of the battery design and its weight. The system level approaches cannot help with the localized hot spots and thermal gradients in the case of thick electrodes. The thermal and electrical gradients within the electrodes can lead to unbalanced charging and discharging resulting in lower energy storage capacity [5]. It has been shown that the thermal effects associated with Li+-ion intercalation – deintercalation can be efficiently addressed by a proper choice of the cathode and anode materials [6]. For these reasons, improving the thermal conductivity of the electrodes themselves is an essential step towards proper thermal management of the batteries. The latter is particularly important for Li+-ion batteries because their performance strongly depends on the electrode temperature [7-9].

Conventional design of the electrodes involves mixing of the active materials with carbon black, conductive additives and polymer binders that provide the integrity for the electrodes and electrical connectivity [10]. The problem with the carbon-black-based electrodes, when used in high-power-density batteries, is their very low thermal conductivity of K~0.1 W/mK – 2 W/mK at room temperature (RT) [11]. Such a low values stem from poor heat conduction properties of amorphous carbon, which K ~ 0.1 – 1 W/mK near RT [11-12], and mechanical-mix-type structure of the electrodes, which introduces high thermal boundary resistance. The low thermal conductivity of the carbon-black-based electrodes leads to their degradation as a result of the undesired thermally activated metal dissolution in cathodes, or degradation of the surface electrolyte interface layer at anode [13-15]. In this Letter, we propose a scalable and inexpensive method for synthesis of the battery electrodes with significantly enhanced thermal conductivity.

Graphene and carbon nanotubes (CNTs) have the highest thermal conductivities of all known materials. The K values for suspended graphene and individual CNTs are in the range from 2000 W/mK to 5000 W/mK at RT [16-19]. They are larger than the thermal conductivity of high-quality single crystal diamond (K~2000 W/mK). Unlike diamond, which is an electrical insulator, graphene and CNTs are electrical conductors and, as such, do not deteriorate electrical conductivity of composite materials. Recent studies indicated that both graphene and CNTs can be used as heat conducting fillers in composite materials [20-23]. Surface functionalization of CNTs, e.g. attachment of certain chemical groups or nanoparticles, can improve their thermal coupling to the composite base material [23]. It was also demonstrated that CNTs by themselves can be

used as the anode material in Li+-ion batteries showing capacities up to 1000 mAh/g [24]. However, such electrodes suffer from the large hysteresis in the voltage profiles between change and discharge states and absence of the voltage plateau that limits their utilization in Li+-ion batteries [24]. The CNT electrodes are also prohibitively expensive.

5.2. Material Synthesis

Hollow γ-Fe2O3 NPs and γ-Fe2O3 NPs on CNTs were synthetized according the synthetic protocols described in Ref. In order to fabricate CNT-based electrodes 4.0 mg of multiwall CNTs were dispersed in 150 mL of isopropyl alcohol (IPA) and sonicated for 5 minutes. After that the suspension of CNTs was filtrated by vacuum through the filter (microporous polyolefin separator Celgard 2325) that served as a separator in electrochemical tests. As a result, a black paper made of CNTs was formed onto the filter. The active layered was fabricated in the same manner: 12.0 mg of electrode material (hollow γ-Fe_2O_3 NPs or $Li[Ni_{1/3}Co_{1/3}Mn_{1/3}]O_2$) mixed with 3 mg of CNTs in IPA were vacuum-filtrated forming of the uniform layer. In case of hollow γ-Fe_2O_3 NPs synthetized on the surface of CNTs we used 15 mg of the material that contained 12.0 mg of γ-Fe_2O_3 NPs and 3 mg of CNTs. After the evaporation of the solvent residue, the CNT-based composite electrodes were annealed in an oven at 200 °C for 12 hours and further used in electrochemical tests without any additional processing. The TEM and SEM inspection of the samples was carried out using JEOL 2100F and JEOL 7500F instruments. The electrochemical tests were performed with the 2032 coin type cells with Li metal foil as

the counter electrodes and 1.2 M $LiPF_6$ in ethylene carbonate/ethyl methyl carbonate (3:7 weight ratio) electrolyte (Tomiyama).

In our approach, we utilize multi-wall CNTs as a matrix for encapsulation of electrochemically active cathode materials to fabricate electrodes for Li+-ion batteries. The electrode material is prepared by the scalable and inexpensive filtration method that we previously developed for sandwiching of nanometer-scale electrochemically active materials [25-26]. The filtration of the CNT suspension and the active cathode materials is carried out in iso-propanol [25]. For the present study we synthesized a set of CNT-enhanced samples with varying layered structure. The sample nomenclature is presented in Table I. The structure of the samples is illustrated in Fig. 5-1. The details of the filtration synthesis procedures, sample structure and battery performance were reported by some of us elsewhere [25]. The similarity in the electrode materials was there three-layer structure and the layer thickness. The scanning electron microscopy (SEM) inspection indicates that the typical average thickness of the three-layered electrode – CNTs/cathode material/CNTs – is ~140 μm (see Fig. 5-2 (a)). The average thickness of each CNT layer was determined to be ~35 μm. The individual MW-CNTs were predominantly aligned parallel to the substrate. The latter has important implications for thermal transport. In addition to electrode materials, we performed thermal conductivity measurements for several reference samples, e.g. layer of CNTs on a substrate.

Sample	Layered Structure	Tests Performed
NP-1	CNTs/{γ-Fe_2O_3 NPs on CNTs}/CNTs	battery capacity; in-plane K; cross-plane K
NP-2	CNTs/{γ-Fe_2O_3 NPs + CNTs}/CNTs	battery capacity; cross-plane K
NP-3	CNTs/{γ-Fe_2O_3 NPs + CNTs}	in-plane K; cross-plane K
NP-4	{CNTs + γ-Fe_2O_3 NPs}	in-plane K; cross-plane K
MP-1	CNTs/{$Li[Ni_{1/3}Co_{1/3}Mn_{1/3}]O_2$+CNTs}/CNTs	battery capacity; cross-plane K
MP-2	CNTs/{$Li[Ni_{1/3}Co_{1/3}Mn_{1/3}]O_2$+CNTs}	in-plane K; cross-plane K
REF-1	CNT bundle	cross-plane K

Table5-1 Nomenclature of the Tested Samples

The variations in the sample layered structure and reference samples allowed us to search for an optimum design from the storage capacity and thermal management point of views. One type of the electrodes contained the hollow γ-Fe_2O_3 nanoparticles (NPs) synthetized directly on CNTs (Fig. 5-2 (b)). The hollow NP refers to structures that have a void inside the iron oxide nano-shell. This void is formed as a result of the coalesence of the iron vacancies during the oxidation of iron. [27] The hollow γ-Fe_2O_3 NPs are ~15 nm large with ~4 nm shell. The γ-Fe_2O_3-NP-on-CNT layer was sandwiched between two layers of CNTs forming the CNTs/{γ-Fe_2O_3-NPs on CNTs}/CNTs structure. This structure was measured to have ~187 mAh/g capacity when cycled in cathode regime (4.5 - 1.5 V), excellent stability (no fading during 300 cycles) and 99.9% Coulombic efficiency (see Fig. 5-3). No current collectors were used in electrochemical tests. The

results of the tests indicated that this electrode (sample NP-1) was the best in terms of its battery cathode performance.

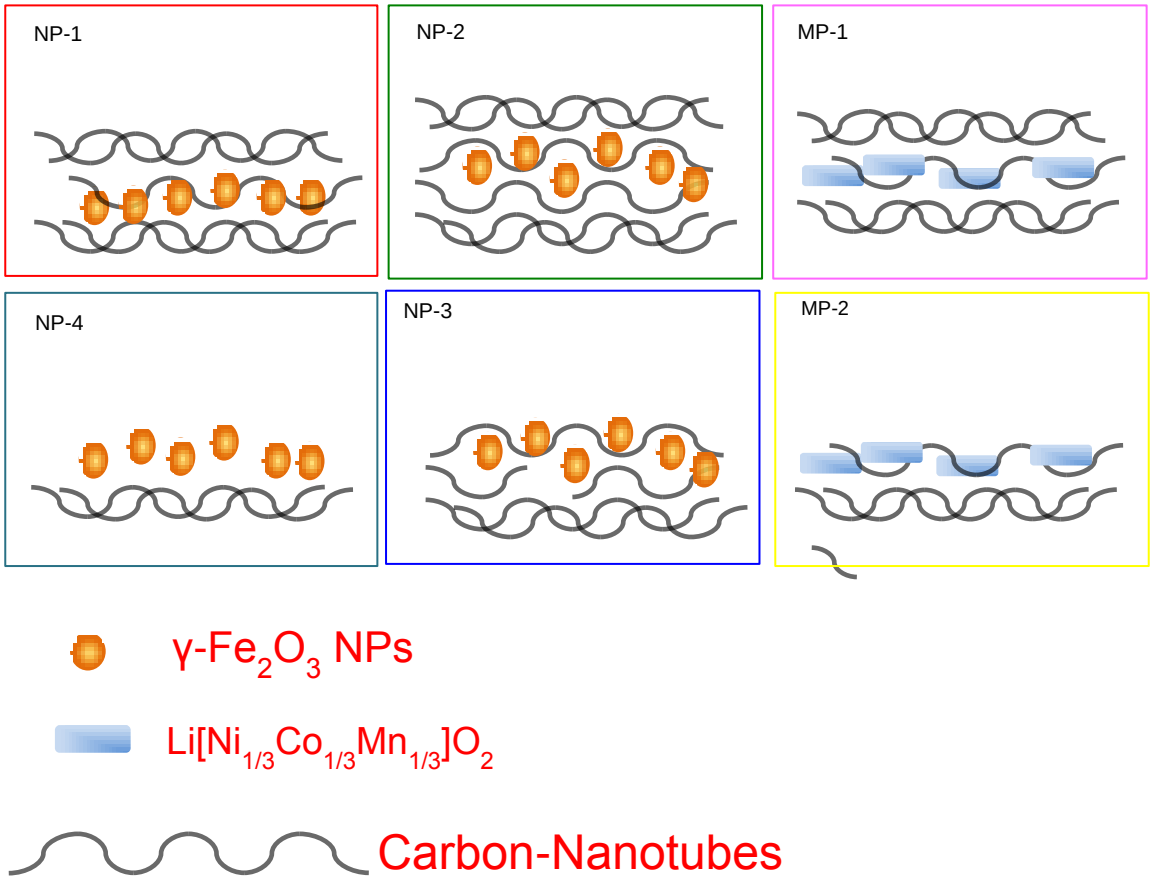

Fig. 5-1 Schematic of the layered structure of the CNT enhanced battery electrodes

5.3. Electrochemical Testing

The cycling of the electrode is accompanied by thermal effects and heat removal may depend on the coupling between the CNTs and electrochemically active γ-Fe_2O_3 NPs. In order to study the effects of coupling of NPs and CNTs on the battery capacity and

thermal conductivity we had a sample NPs were mixed with CNTs (not synthesized on them). The mixed CNT-NP layer was sealed between two layers of CNTs forming CNTs/{hollow γ-Fe_2O_3 NPs + CNTs}/CNTs structure (sample D). As seen in Fig. 5-3, the electrochemical performance of this electrodes (capacity 130 mAh/g) was not as good as that of the electrodes that contained γ-Fe_2O_3 NP synthesized on CNTs (130 mAh/g vs. 187 mAh/g).

A distinctively different type of electrodes utilized $Li[Ni_{1/3}Co_{1/3}Mn_{1/3}]O_2$ microparticles (MP) [28]. The mixture of CNTs and $Li[Ni_{1/3}Co_{1/3}Mn_{1/3}]O_2$ MPs was sandwiched between two layers of CNTs by the filtration method forming CNTs/{$Li[Ni_{1/3}Co_{1/3}Mn_{1/3}]O_2$ + CNTs}/CNTs layers (sample MP-1). The thickness of the

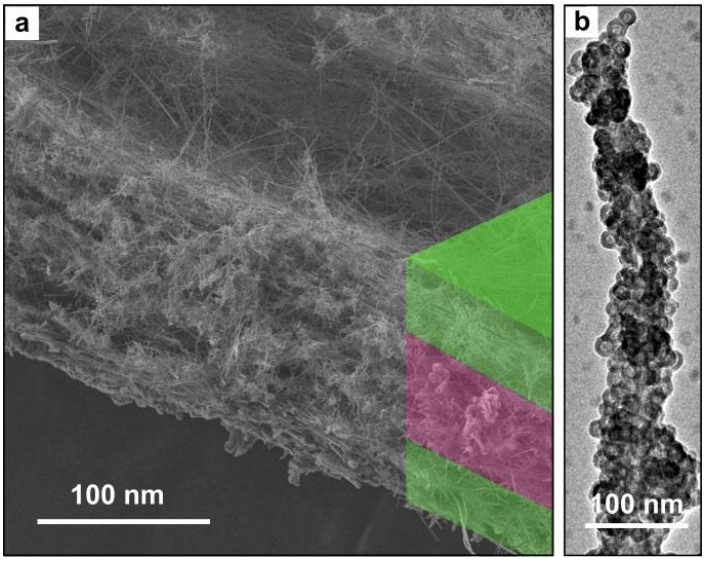

layers was similar to that in the

Fig. 5-5-2 Scanning electron microscopy image of the cross-section of the CNT enhanced battery electrodes. Note that CNTs are predominantly oriented along the sample plane. (b) Scanning electron microscopy image showing nanoparticles grown on CNTs.

NP-based electrodes. The electrochemical tests indicated that such electrodes have a lower capacity (see Fig. 5-3) as compared to NP-based electrodes. However, their cycle stability was significantly higher. No capacity fading was observed up to 800 cycles while ~25-28% capacity loss after 50 cycles was reported for the same cathode material fabricated via a conventional method. The capacity of this battery increased upon cycling up to 50 cycles and then stabilized. The stable performance is an attractive feature of CNT-enhanced electrode designs. After the electrochemical characteristics of the electrodes were determined we proceeded with the thermal measurements.

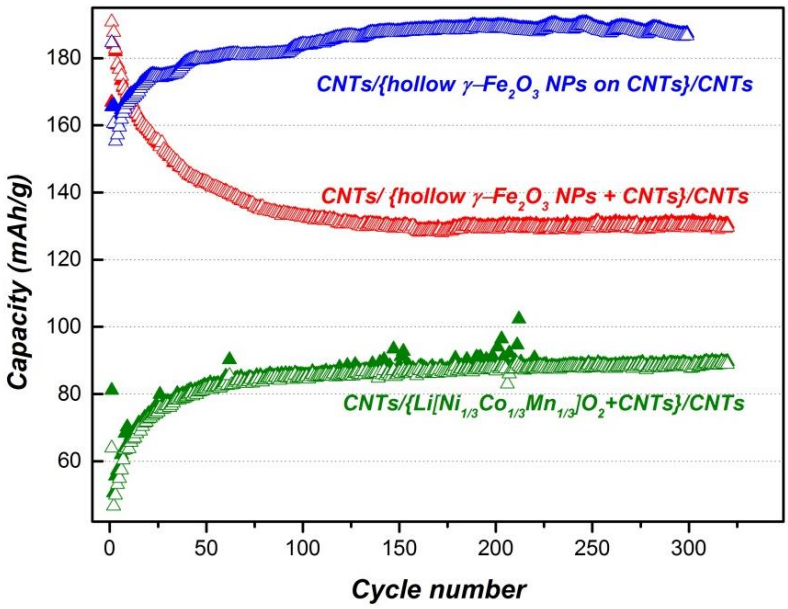

Fig. 5-5-3 Electrochemical Testing of CNT enhanced Li-Ion electrodes

5.4. Thermal Characterization

The thermal conductivity of the samples was determined using two different techniques: “laser flash” and “hot disk”. Owing to the complicated structure of the samples and the “hot disk” equipment limitations, the in-plane thermal conductivity was measured at RT only. The cross-plane thermal conductivity was determined in the range from 290 K to 350 K using the “laser flash” method. The details of the measurement procedures are given in the Methods section. The cross-plane thermal conductivity as a function of temperature for a set of examined electrodes in shown in Fig. 5-4. One can see that the thermal conductivity values are in the range from ~0.5 W/mK to ~10 W/mK. The cross-plane thermal conductivity defines the heat transport through the electrode, i.e. perpendicular to the sample substrate. Although the overall values are not significantly enhanced, many of them are higher than those in conventional electrodes [16]. The strong increase in cross-plane thermal conductivity is not expected because CNTs are predominantly oriented in-plane (along the substrate). In addition, the layered structure of the electrodes results in substantial thermal interface resistance between the layers, e.g. between CNT layer and the γ-Fe2O3 NPs + CNTs layer or between CNT layer and the substrate. The thermal conductivity increases slightly with the temperature or stays approximately constant. Such dependence is expected for material systems with large decree of disorder.

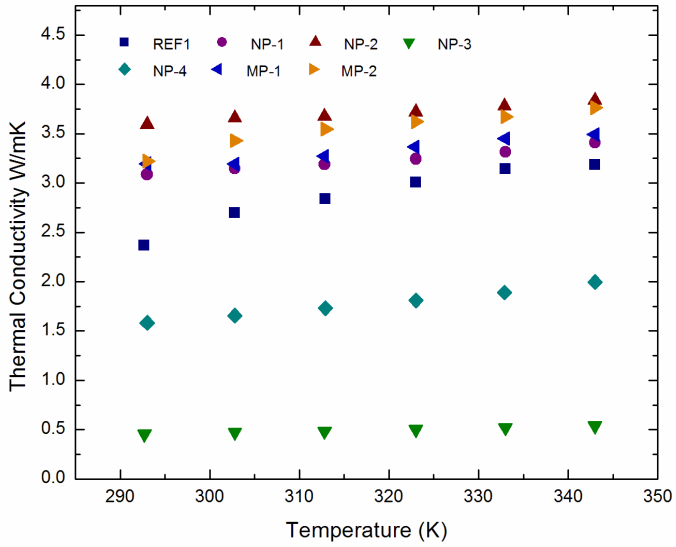

Fig. 5-4 Cross plane Thermal Conductivity of CNT enhanced Li-Ion Electrodes

Fig. 5-5 shows in-plane and cross-plane thermal conductivity for a set of different samples at RT. One can see that the in-plane thermal conductivity is substantially higher than the cross-plane. This is explained by the predominantly in-plane (along the substrate) orientation of CNTs. The in-pane values range from 50 W/mK to 141 W/mK. The NP-1 sample, which had the best electrochemical performance, revealed the thermal conductivity of 50 W/mK. This value is about two orders of magnitude higher than the thermal conductivity of the conventional carbon black based electrodes [29] and at least two times higher than the in-plane thermal conductivity of the Sony Li+-ion electrodes with engineered controls for heat removal [30]. In general, the NP-based electrodes had higher thermal conductivity than the MP-based electrodes, which was attributed to the higher mass density of NP-based samples. The measured in-plane thermal conductivity

values for these electrodes were typically in-line with the reported data for CNT bundles, i.e. *K*~50 W/mK. The thermal conductivity of NP-4 electrode, K=141 W/mK, is somewhat higher than the values typically reported for the CNT bundles [31].

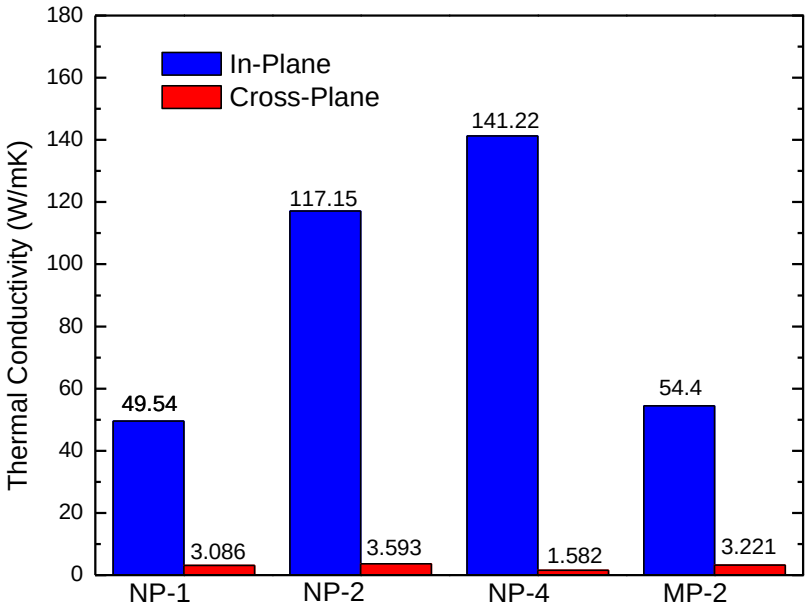

Fig. 5-5 In-plane and cross-plane thermal conductivity for a set of different samples at RT

The cross-plane thermal conductivity is in the range from 1.6 W/mK to 3.6 W/mK. The electrode with the best electrochemical performance, revealed the thermal conductivity value of 3.1 W/mK at RT. This value is about an order of magnitude higher than that of the carbon-black based electrode materials [32]. It is also higher that the cross-sectional thermal conductivity of the electrodes of commercial Sony Li+-ion batteries, i.e. 2.33 W/mK and 0.89 W/mK, for positive and negative electrodes, respectively [30]. The

measured data indicate that most of tested CNT enhanced electrodes revealed substantially enhanced in-plane and cross-plane thermal conductivity as compared to electrodes synthesized by the conventional techniques. Even though the enhancement is not as high as in the electrodes based on ordered CNT arrays [12]. However, our electrodes were fabricated by the inexpensive scalable filtration method [25], which can be extended to commercial electrode-active materials while the fabrication of ordered CNT arrays is still prohibitively expensive. The systematic study of thermal properties of CNT enhanced samples did not show a clear correlation with the specifics of the layered structure. .

We reported the thermal properties of Li-ion battery electrodes enhanced with multi-wall CNTs. The electrodes were synthesized via an inexpensive scalable *filtration* method. Our measurements indicate that the CNT enhanced electrodes reveal up to *two-orders-of-magnitude* enhancement of the thermal conductivity. The in-plane thermal conductivity in some electrodes reached ~141 W/mK at RT. The described approach for increasing the thermal conductivity can be extended to commercial electrode-active materials. The obtained results are important for thermal management of Li-ion and other high-power-density batteries.

5.5. References

[1] A. S. Arico, P. Bruce, B. Scrosati, J.-M. Tarascon, W. van Schalkwijk, Nat. Mater. 2005, 4, 366.

[2] Linden, D., Reddy, B.T. (2002) Handbook of Batteries. McGraw-Hill, New York.

[3] Spotnitz, R., Franklin, J. (2003) Abuse behavior of high-power, lithium-ion cells. Journal of Power Sources (Elsevier) 113, 81–100.

[4] J. Y. Huang, L. Zhong, C. M. Wang, J. P. Sullivan, W. Xu, L. Q. Zhang, S. X. Mao, N. S. Hudak, X. H. Liu, A. Subramanian,1 H. Fan, L. Qi, A. Kushima, J. Li. Sci., 330:1515, 2010.

[5] Garimella, S. V., Fleischer, A. S., Murthy, J. Y., Keshavarzi, A., Prasher, R., Patel, C., Bhavnani, S. H., Venkatasubramanian, R., Mahajan, R., Joshi, Y., Sammakia, B., Myers, B. A., Chorosinski, L., Baelmans, M., Sathyamurthy, P., Raad, P. E. (2008) Thermal Challenges in Next-Generation Electronic Systems. IEEE Trans. Compon. Packag. Technol. 31, 801−815, 2008.

[6] Y. Oumella, A. Rougier, G. A. Nazr, J. M. Tarascon, L. Aymard. Nat., 7:916, 2008.

[7] G.G. Amatucci, C. N. S., A. Blyr, C. Sigala, A.S. Gozdz, D. Larcher, J.M. Tarascon. Materials' effects on the elevated and room temperature performance of C/LiMn204 Li-ion batteries. Journal of Power Sources 69, 1-25 (1997).

[8] S.S. Zhang, K. X., T.R. Jow. The low temperature performance of Li-ion batteries. Journal of Power Sources 115, 137-140 (2003).

[9] Yan Ji, Y. Z., Chao-Yang Wang Li-Ion Cell Operation at Low Temperatures. Journal of The Electrochemical Society 160, A636-A649 (2013).

[10] L. Fransson, T. E., K. Edstrom, T. Gustafsson, J. O. Thomas. Influence of carbon black and binder on Li-ion batteries. Journal of Power Sources 1101, 1-9 (2001).

[11] H. Maleki, S A Hallaj, J. R. Selman, R. B. Dinwiddie and H. wang. “Thermal properties of lithium ion batteries and components”, J. Elect.Chem.Soc., 146,3,647,1999.

[12] Kara Evanoff, J. K., Alexander Balandin, Alexandre Magasinski, W. Jud Ready, Thomas F. Fuller, Gleb Yushin. Towards Ultrathick Battery Electrodes: aligned Carbon Nanotube-Enabled Architecture. Adv. Mat. 24, 533-537 (2012).

[13] J. Vetter, P. N., M.R. Wagner, C. Veit, K.-C. Möller, J.O. Besenhard, M. Winter, M. Wohlfahrt-Mehrens, C. Vogler, A. Hammouche. Ageing mechanisms in lithium-ion batteries. J. Power Sources 147, 269-281 (2005).

[14] Todd M. Bandhauer, S. G., Thomas F. Fuller. A Critical Review of Thermal Issues in Lithium-Ion Batteries. J. Electrochem. Soc. 158, R1-R25 (2011).

[15] P. Ramadass, B. H., Parthasarathy M. Gomadam, Ralph White, Branko N. Popov. Development of First Principles Capacity Fade Model for Li-Ion Cells. J. Electrochem. Soc. 151, A196-A203 (2004).

[16] A.A. Balandin, "Thermal properties of graphene and nanostructured carbon materials," Nature Materials, 10, 569 - 581 (2011).

[17] D.L. Nika, A.S. Askerov and A.A. Balandin "Anomalous size dependence of the thermal conductivity of graphene ribbons," Nano Letters, 12, 3238 (2012).

[18] D.L. Nika and A.A. Balandin, "Two-dimensional phonon transport in graphene," Journal of Physics: Condensed Matter, 24, 233203 (2012).

[19] K.M.F. Shahil and A.A. Balandin, "Thermal properties of graphene and multilayer graphene: Applications in thermal interface materials," Solid State Communications, 152 , 1331 (2012).

[20] K.M.F. Shahil and A.A. Balandin, "Graphene - multilayer graphene nanocomposites as highly efficient thermal interface materials," Nano Letters, 12, 861 (2012).

[21] V. Goyal and A.A. Balandin, "Thermal properties of the hybrid graphene-metal nano-micro-composites: Applications in thermal interface materials," Applied Physics Letters, 100, 073113 (2012).

[22] P. Goli, S. Legedza, A. Dhar, R. Salgado, J. Renteria and A.A. Balandin, "Graphene-enhanced hybrid phase change materials for thermal management of Li-ion batteries," Journal of Power Sources, X (2013).

[23] R. Gulotty, M. Castellino, P. Jagdale, A. Tagliaferro and A.A. Balandin, "Effects of functionalization on thermal properties of single-wall and multi-wall carbon nanotube polymer nanocomposites," ACS Nano, 7, 5114 (2013).

[24] Ray H. Baughman, A. A. Z., Walt A. de Heer. Carbon Nanotubes--the Route Toward Applications. Science 297, 787-792 (2002).

[25] Koo, B. et al. Intercalation of Sodium Ions into Hollow Iron Oxide Nanoparticles. Chemistry of Materials 25, 245-252, doi:10.1021/cm303611z (2013).

[26] Koo, B. et al. Hollow Iron Oxide Nanoparticles for Application in Lithium Ion Batteries. Nano Lett. 12, 2429-2435, doi:10.1021/nl3004286 (2012).

[27] Cabot, A., Puntes, V.F., Shevchenko, E., Yin, Y., Balcells, L., Marcus, M.A., Hughes, S.M., Alivisatos, A.P. Vacancy Coalescence during Oxidation of Iron Nanoparticles. J. Am. Chem. Soc. 129, 10358-10360 (2007).

[28] Seung-Taek Myung, K.-S. L., Chong Seung Yoon, Yang-Kook Sun, Khalil Amine, Hitoshi Yashiro. Effect of AlF3 Coating on Thermal Behavior of Chemically Delithiated Li0.35[Ni1/3Co1/3Mn1/3]O2. J. Phys. Chem. C 114, 4710-4718 (2010).

[29] Li Song, J. W. E. Measurements of the Thermal Conductivity of Lithium Polymer Battery Composite Cathodes. . J. Electrochem. Soc. 146, 869-871 (1999).

[30] Hossein Malekia, S. A. H., J. Robert Selmana, Ralph B. Dinwiddieb, H. Wangb. Thermal Properties of Lithium-Ion Battery and Components. J. Electrochem. Soc. 146, 947-954 (1999).

[31] Da Jiang Yang, Q. Z., George Chen, S. F. Yoon, J. Ahn, S. G. Wang, Q. Zhou, Q. Wang, J. Q. Li Thermal conductivity of multiwalled carbon nanotubes. Phys. Rev. B 66 (2002).

[32] Li Song, J. W. E. Measurements of the Thermal Conductivity of Lithium Polymer Battery Composite Cathodes. Journal of the Electrochemical Society 146, 869-871 (1999).

[33] Gustafsson, S. E. (1991) Transient plane source techniques for thermal conductivity and thermal diffusivity measurements of solid materials , Rev. Sci. Instrum. 62(3), 797.

[34] Gustafsson, S. E., Karawacki, E., Chohan, M. A. (1986) Thermal transport studies of electrically conducting materials using the transient hot-strip technique. J. Phys. D 19, 727.

[35] Gustafsson, M., Wang, H., Trejo, R. M., Lara-Curzio, E., Dinwiddie, R. B., Gustafsson, S. E. (2006) On the Use of the Transient Hot-Strip Method for Measuring the Thermal Conductivity of High-Conducting Thin Bars. Int. J. Thermophys. 27, 1816.

Chapter VI

Graphene Coating of Prototype Cu Interconnects

6.1. Introduction

Graphene[3] is a one-atom-thick material with unusual and highly promising for applications electrical [1-3], thermal [4-5] and mechanical properties [6]. First obtained by mechanical exfoliation from graphite [1-2], graphene is now efficiently grown by chemical vapor deposition (CVD) on copper (Cu) films [7-9]. It was reported that layered graphene – metal composites have enhanced mechanical strength [10]. However, it is still not known how the deposition of graphene on Cu films affects the thermal properties of the resulting graphene – Cu films. The knowledge of thermal properties of graphene – Cu "sandwiches" is important for the following practical reasons. Copper became the crucial material for interconnects in silicon (Si) complementary metal-oxide-semiconductor (CMOS) technology by replacing Al. Main challenges with continuous downscaling of Si CMOS technology include electromigration in Cu interconnects, Cu diffusion to adjacent layers and heat dissipation in the interconnect hierarchies separated from a heat sink by many layers of dielectrics [11]. Combining graphene and Cu in some sort of hybrid heterogeneous global interconnect can bring potential benefits of reducing Cu electromigration and diffusion. It has already been demonstrated that the breakdown current density in prototype graphene interconnects can exceed that in metals by $\times 10^3$ [12]. Graphene capping of Cu interconnects increases the current density and reduces electrical resistance [13]. Intersecting hybrid graphene – Cu interconnects have been shown to offer benefits for downscaled electronics [14-15]. Increasing the heat

[3] Partially reprinted from P. Goli, X. Li, C. Y. Lu, K. S. Novoselov and A. A. Balandin, Strong Enhancement of Thermal Properties of Copper Films after Chemical Vapor Deposition of Graphene", Nanoletters, ASAP 2014.

conduction properties of Cu films with graphene coating could become a crucial added benefit for improving the thermal management of the interconnect hierarchies.

Graphene is known to have usually high intrinsic thermal conductivity, which can exceed that of bulk graphite limit of K≈2000 W/mK at RT in sufficiently large high-quality samples [4-5]. However, graphene placement on substrates results in degradation of thermal conductivity to ~600 W/mK owing to phonon scattering on the substrate defects and interface [16]. The benefits of using single-layer graphene (SLG) or few-layer graphene (FLG) as heat spreaders for large substrates are not obvious owing to the small thickness of graphene (h=0.35 nm) and possible thermal conductivity degradation by extrinsic effects. Even if K is high, the uniform heat flux, $\Phi=K\times A$, through the cross-sectional area $A=hW$ will be small due to small h (W is the width of the graphene layer).

We report the results of our thermal measurements that demonstrate that CVD of graphene on both sides of Cu films enhances the thermal diffusivity, α, and thermal conductivity, K, of the resulting graphene – Cu – graphene (Gr-Cu-Gr) hetero-films. Deposition of graphene increases K of 9-μm (25-μm) thick Cu films by up to 24% (16%) near room temperature (RT). Interestingly, the enhancement of thermal properties of Gr-Cu-Gr hetero-films is primarily due to changes in Cu morphology during graphene deposition rather than graphene's action as an additional heat conducting channel. Specifically, CVD of graphene results in strong enlargement of Cu grain sizes and reduced surface roughness. A typical grain size in Cu films coated with graphene is larger

than that in reference Cu films and in Cu films annealed under the same conditions without graphene deposition.

To demonstrate the effect we used a set of Cu films (thickness H=9 μm and H=25 μm) with SLG and FLG synthesized on both sides via CVD method (Bluestone Global Tech, Ltd.). As references we used (i) Cu films without graphene or any thermal treatment, and (ii) Cu films annealed under the same conditions as the one used during CVD of graphene. Thus, for comparison we had regular Cu, annealed Cu, Cu with CVD SLG and Cu with CVD FLG. Details of sample preparation are provided in *Methods* section. The reference Cu and Cu-graphene samples were subjected to optical microscopy, scanning electron microscopy (SEM) and atomic-force microscopy (AFM) inspection. The number of atomic planes in graphene films on Cu was verified with micro-Raman spectroscopy (Renishaw In Via). Details of our Raman measurement procedures have been reported by some of us elsewhere [17].

6.2. Sample Preparation and Characterization

Graphene was synthesized in a low-pressure CVD system. A copper substrate was heated up to 1030 ^{o}C under hydrogen and then methane was introduced for graphene growth. The samples with SLG and FLG were synthesized by controlling the cooling rate. For the case of SLG, the copper substrate was cooled from 1030 ^{o}C to RT within 20 minutes while for FLG the cooling time was about 10 hours. The annealing of copper for reference samples was performed with the same heating and cooling process as that of SLG synthesis but no methane addition during the process. We performed extensive

scanning electron microscopy (SEM) and atomic force microscopy (AFM) study to inspect the thickness and roughness of the samples (see Fig. 6.1).

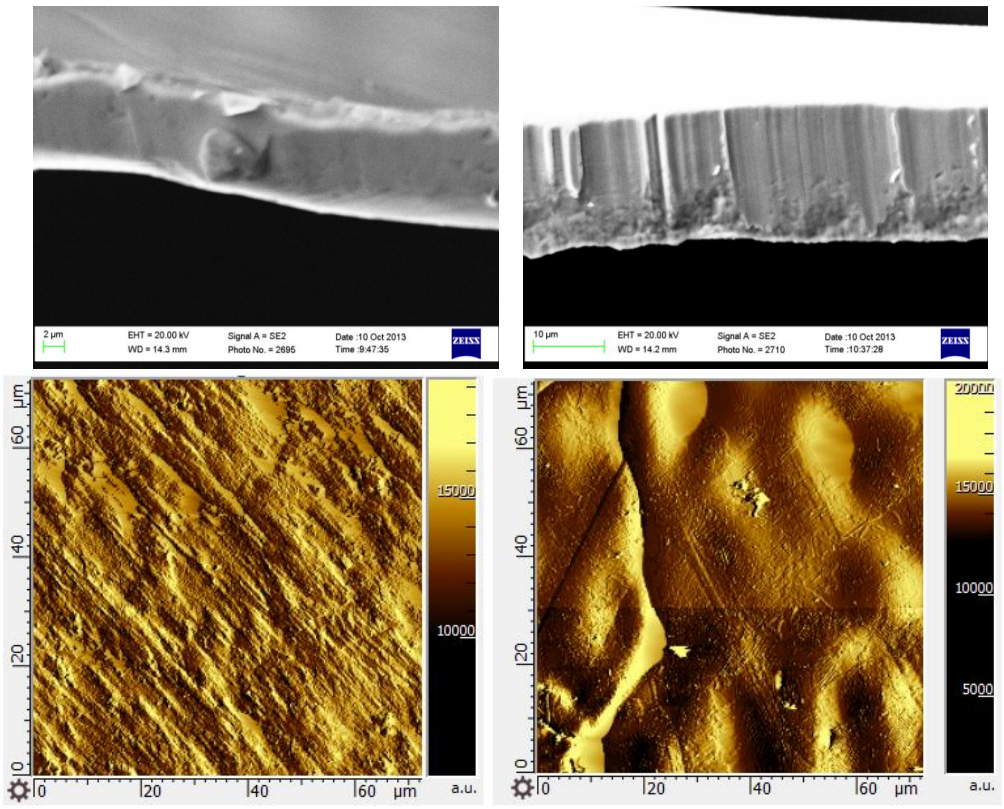

Fig. 6-1 SEM image of the cross-section of the annealed 9-µm thick Cu film (top left panel) and 25-µm thick Cu films with few-layer graphene (top right panel). AFM image of 9-µm thick Cu film (bottom left panel) and 9-µm thick Cu films with single-layer graphene (top right panel).

The purity of 25-µm thick copper is 99.9 % and that of 9-µm thick copper is above 99.99 %. Graphene is synthesized in a low-pressure CVD system following the method described in Refs. [7-8]. A copper substrate is heated up to 1030^{o}C under hydrogen and

then methane is introduced for graphene growth. The samples with SLG and FLG are synthesized by controlling the cooling rate. For the case of SLG, the copper substrate is cooled from 1030^{o}C to RT within 20 minutes while for FLG the cooling time is about 10 hours. The annealing of copper for reference samples is performed with the same heating and cooling process as that of SLG synthesis but no methane addition during the process. The annealing time was kept at 20 minutes.

In order to check the sample composition we performed X-ray photoelectron spectroscopy (XPS) after CVD of graphene and after annealing of the reference samples.

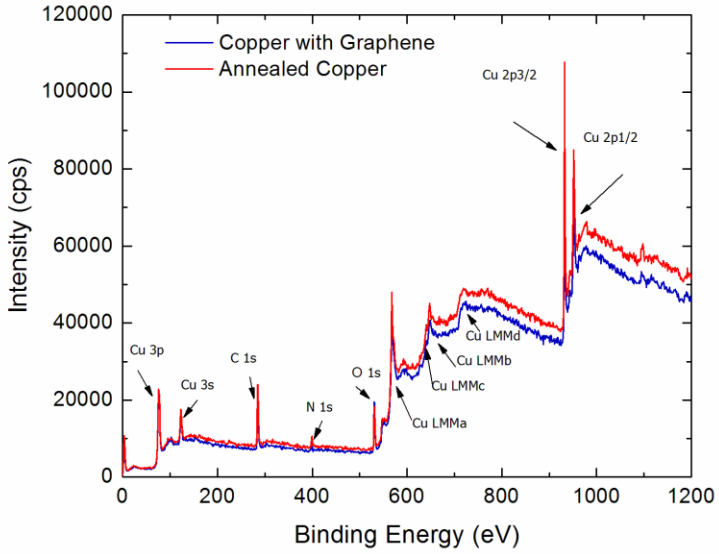

XPS is a surface-sensitive quantitative spectroscopic technique that measures the elemental composition (see Fig. 6.2). It was established that the impurity composition (O, N) do not differ in Cu with graphene and annealed Cu. The oxygen content has not changed after annealing or graphene deposition. The latter indicates that the change in the impurity

Fig. 6-2 XPS data for the 9-μm thick annealed Cu film and Cu film with graphene.

composition is not responsible for the observed change in the thermal conductivity. We have also performed energy-dispersive X-ray spectroscopy (EDX) for verifying the elemental composition of the samples. Similarly, the data did not indicate any substantial deviation in the composition of Cu after CVD of graphene and after annealing, which could be interpreted as responsible for the thermal conductivity changes.

The measurements of the thermal diffusivity were carried out using the "laser flash" method (Netzsch LFA). In conventional configuration, the "laser flash" method gives the cross-plane thermal diffusivity, α, of the sample [18]. Since we are mostly interested in the in-plane heat spreading properties of Gr-Cu-Gr hetero-films, we altered the experiment by using a special sample holder, which send the thermal energy along the sample. In this approach, the location for the light energy input on one side of the sample and location for measuring the temperature increase on the other side of the sample are at different lateral positions. The latter insures that the measured temperature increase of the sample corresponds to the thermal diffusivity in the in-plane direction. The thermal conductivity was determined from the equation $K=\rho\alpha C_p$, where ρ is the mass density of the sample and C_p is the specific heat of the sample measured separately. Details of the measurements are summarized in *Methods* section. Fig. 6.3 presents a schematic of the experiment, an image of a typical sample with the sample holder, and Raman spectra from two different Cu substrates indicating that one has SLG coating while the other has FLG coating. The average thickness of FLG was five atomic planes.

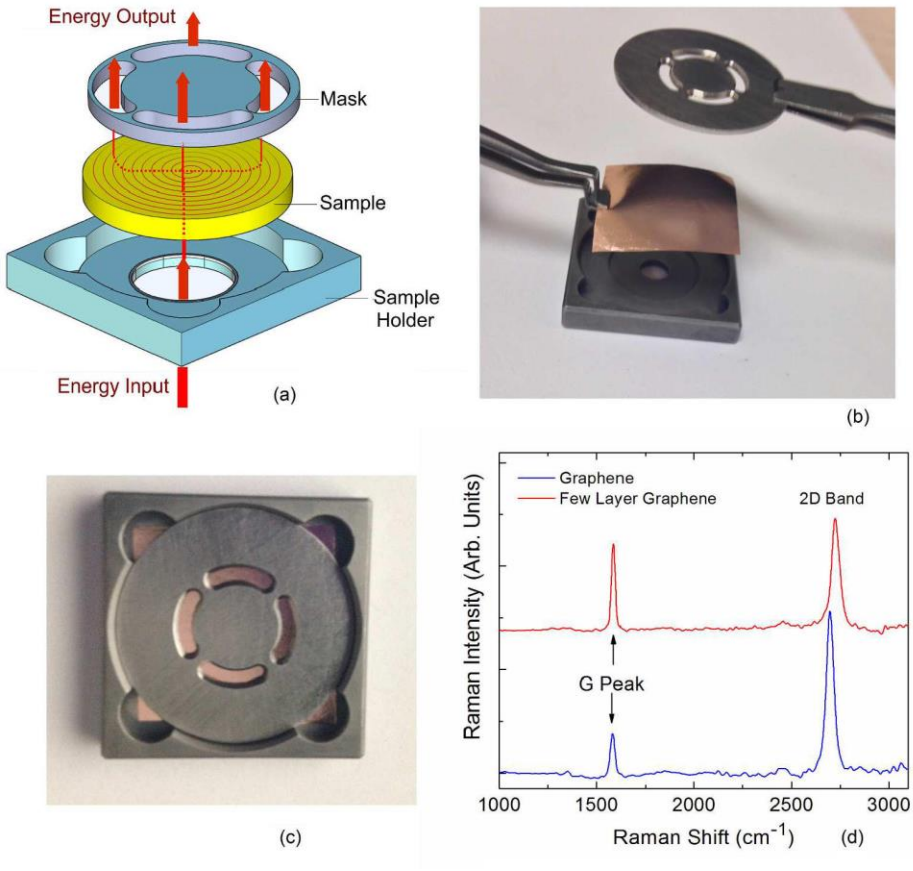

Fig. 6-3 Samples and the measurement setup. (a) Schematic of the modified "laser flash" experimental setup for measuring in-plane thermal diffusivity. (b) Cu film coated with CVD graphene placed on the sample holder. (c) Back side of the sample holder with the slits for measuring temperature. Cu film is seen through the openings. (d) Raman spectrum of graphene and few-layer graphene on Cu. The data is presented after background subtraction.

6.3. Thermal Characterization

The thermal diffusivity and specific heat were measured by the "laser flash" technique (LFT). The design of the "in-plane" sample holder ensured that heat traveled ~5 mm inside Cu film along its plane, which is a much larger distance than its 25 μm thickness. The latter ensured the in-plane values for α and K. The temperature rise as a function of time, $\Delta T(t)$, was used to extract α. An example of measured of thermal diffusivity of two different Cu films with FLG is shown in Fig. 6.4. The thermal diffusivity of Cu film before CVD of FLG is also presented for comparison.

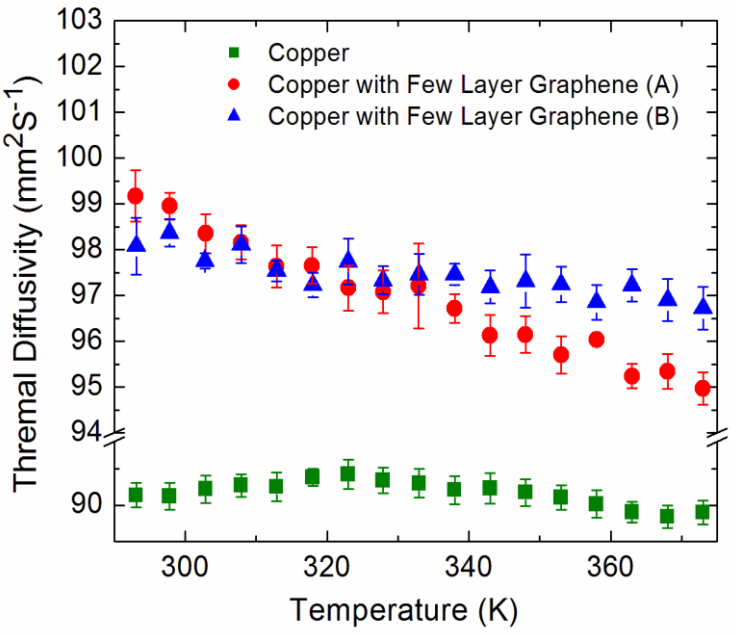

Fig. 6-4 Thermal diffusivity as a function of temperature for two different Cu films with FLG and reference Cu film. The Cu films thickness is H=25 µm.

The specific heat, C_p, was measured with LFT by comparing ΔT of the sample to that of a reference sample under the same experimental conditions. The specific heat is defined as

$C_p=Q/m\Delta T$, where m is the mass of the material, ΔT is the change in temperature, and Q is the energy required to raise a unit mass of the material by one unit of temperature under constant pressure. The specific heat is measured by LFT by comparing the temperature rise of the sample to the temperature rise of the reference sample of known specific heat tested under the same conditions. The temperature rise is defined in the instrument by the voltage rise. For the conditions when the light pulse energy and its coupling to the sample remain unchanged between the examined and referenced sample, the absorbed energy $Q=(mC_p\Delta T)_r=(mC_p\Delta T)_s$ where the subscript "*r*" stands for reference and subscript "*s*" stands for sample. The specific heat of the sample under study was determined as $(C_p)_r=(mC_p\Delta T)_r/(m\Delta T)_s=(mC_p\Delta V)_rG_s/((m\Delta V)_sG_r)$, where ΔV is output voltage of the IR detector and G is the detector amplifier gain. The reference sample is measured at each temperature of interest to calibrate the change in the output voltage ΔV resulting from the absorbed light energy. The measured ΔV divided by the detector amplifier gain is proportional to the temperature rise provided that the temperature rise is small. The measured DV is affected by the heat loss during the measurement. In order to use the above equation, the heat loss factors of the reference and test sample should be similar. For this reason, in our measurements Cu was used as the standard reference. The absorptive efficiency of the front surface of the sample to the light pulse and radiative efficiency of the of the back surface to the IR detector have been controlled by the standard method of coating the light input opening for the reference and test sample with the same thin layer of graphite. Fig. 6.5 shows an representative plot of the specific heat

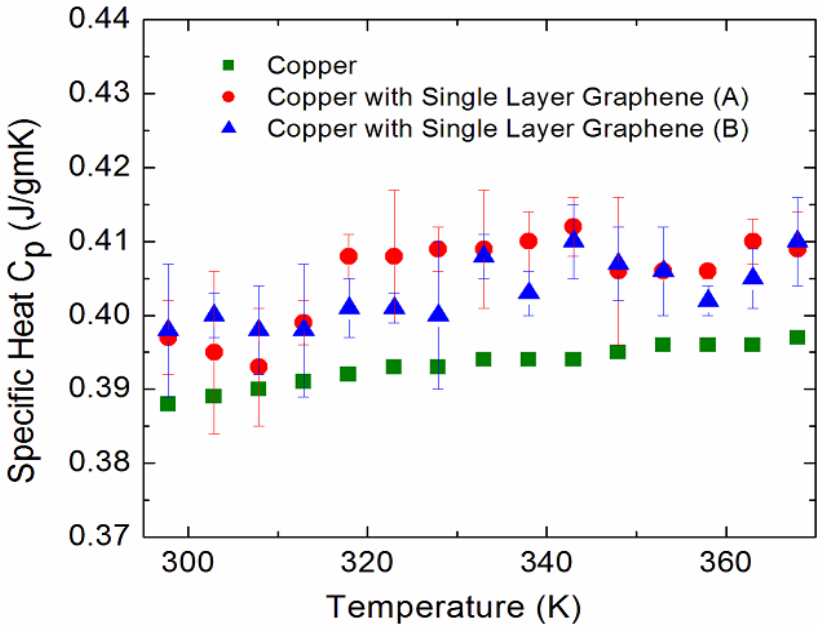

for Cu films with SLG. The thermal conductivity was determined from the equation $K=\rho\alpha C_p$, where ρ is the mass density of the sample.

Fig. 6-5 Specific heat as a function of temperature for two different Cu films with FLG and reference Cu film. The Cu films thickness is H=25 μm

Fig. 6.6 presents the average apparent thermal diffusivity and thermal conductivity in reference Cu films, annealed Cu films, Cu films with CVD graphene and Cu films with CVD FLG. The data are presented for two thicknesses of Cu films: H=25 μm and H=9 μm. The term *apparent* (another common term is *effective*) emphasizes that α and K values are measured for the whole graphene-Cu-graphene sample. The averaging for each type of sample (e.g. Cu film with SLG) was performed for five locations on each film at each temperature. Two films with the same type of samples were tested. In order to simplify the analyses, in Table I, we provided the average RT values of $\alpha$and K measured for different samples and locations. The ranges for α and K values for different locations

and samples are given in the brackets. The data scatter for different locations was attributed to the sample non-uniformity and film bending, which were unavoidable for large foils (cm scale lateral dimensions) with small thicknesses.

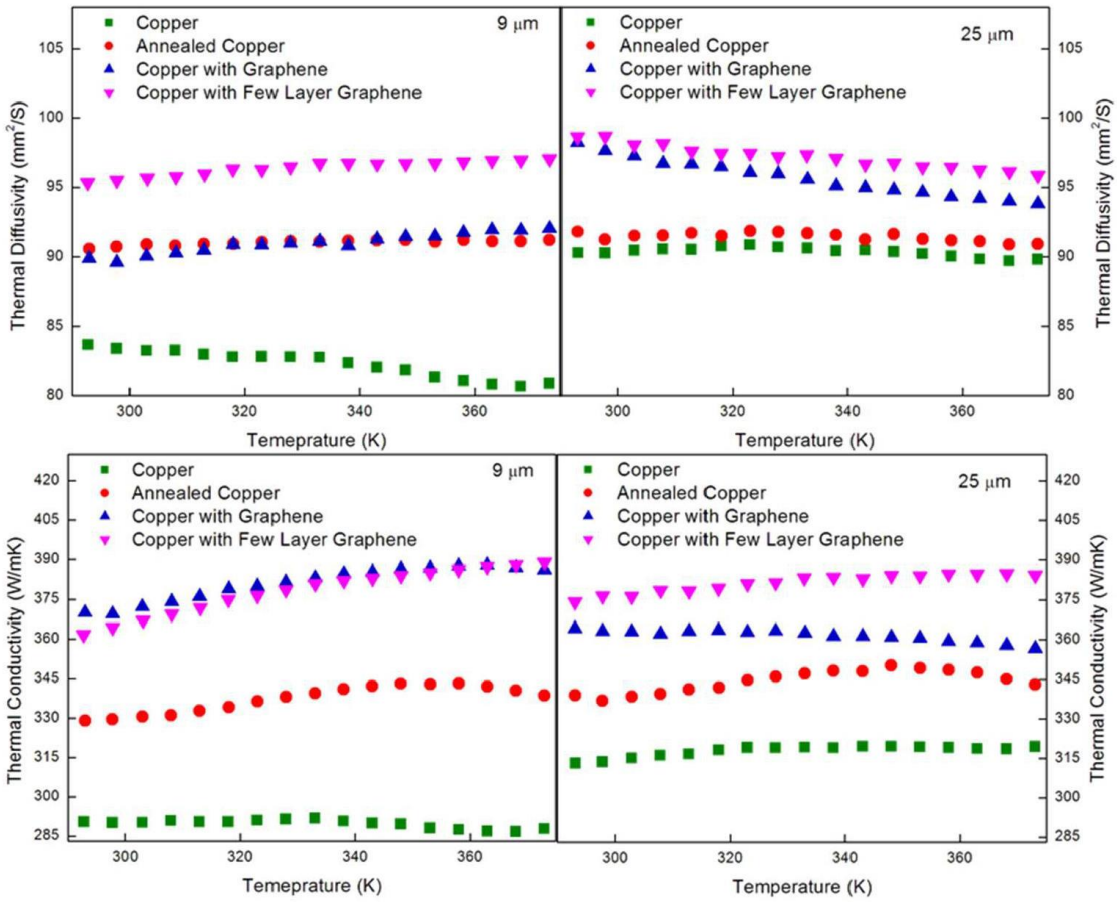

Fig. 6-6 Thermal diffusivity of reference Cu film, annealed Cu, Cu with CVD graphene, and Cu with CVD FLG (top panels). Thermal conductivity of reference Cu film, annealed Cu, Cu with CVD graphene, and Cu with CVD FLG (bottom panels). The data are shown for Cu films with H=9 μm and H=25 μm. Note that CVD of graphene and FLG results in stronger increase in the apparent thermal conductivity of graphene-Cu-graphene samples than annealing of Cu under the same conditions.

Cu samples	9 μm	9 μm annealed	9 μm with SLG	9 μm with FLG	25 μm	25 μm annealed	25 μm with SLG	25 μm with FLG
α (mm^2S^{-1})	84	90.7 (87 – 93)	89.6 (88 – 93)	95.5 (91 – 99)	90	91.2 (91 – 92)	97.6 (95 – 100)	98.4 (98 – 99)
K (W/mK)	290	329.5 (319 – 340)	369.5 (361 – 379)	364.3 (346 – 378)	313	337.2 (320 – 358)	363.0 (354 – 374)	376.4 (372 – 377)
$\Delta\alpha/\alpha$ (%)	–	7.4	6.3	12.0	–	1.3	7.8	8.5
$\Delta K/K$ (%)	–	11.9	21.5	20.4	–	7.2	13.8	16.9

Table 6-1 Thermal Diffusivity and Thermal Conductivity of Graphene Coated Cu Films

The obtained α and K of Gr-Cu-Gr hetero-films and their weak temperature dependence are consistent with literature values for bulk Cu, which varies from 385 W/mK to 400 W/mK [19-21]. As reported in Refs. [20-21], in the relevant temperature range of 300 K – 400 K, the thermal conductivity of copper slightly decreases (increases) in bulk (thin films with H≈40 nm – 200 nm range) with temperature. The latter is explained by the interplay of the intrinsic and boundary scattering mechanisms for the heat carriers [19-

21]. In terms of their thickness our samples fall in between these two limiting cases. The latter explains the observed weak and sometimes non-monotonic dependence of the thermal conductivity on temperature.

Electrons are the main heat carriers in Cu while phonons make the dominant contribution in graphene. The strong reduction of K of Cu due to electron scattering from the film top and bottom boundaries is only expected in very thin films where the electron mean-free path (MFP) becomes comparable with H [21]. However, it is known that the grain size in Cu decreases with the decreasing film thickness [20]. For this reason, the size effects can reveal themselves even in relatively thick Cu films with $H \leq 10$ μm [20]. The lower α and K for 9 μm films than those for 25 μm films measured in our experiments are likely related to the grain size effects. The rolling fabrication of Cu films of different thickness (9 μm vs. 25 μm) is also expected to result in variations in the defect densities, grain elongation and orientation, thus, affecting α and K.

The most important and unexpected observation from Fig. 6.7 is that α and K are strongly increased in Gr-Cu-Gr hetero-films with graphene or FLG coating compared to reference Cu films or annealed Cu films. Deposition of graphene results in stronger increase of α and K than annealing under the same conditions. In terms of thermal conductivity, the effect of graphene deposition is particularly pronounced for thinner Cu films (H=9 μm). The deposition of SLG on 9-μm Cu film results in about ~22% enhancement of the apparent thermal conductivity as compared to ~12% increase in the annealed samples without graphene. The average enhancement of K and α after deposition of SLG on 25-

μm films is less pronounced than that for 9-μm films but still notably larger than for the annealed reference samples. The increase in α and K is not proportional because the thermal treatment during CVD or annealing affects the specific heat as well. It is known that thermal treatment of metals and alloys can noticeably change C_p, particularly in the presence of impurities and defects [22].

The overall enhancement of heat conduction properties of Gr-Cu-Gr hetero-films as compared to reference Cu films is very strong and may appear puzzling. The thickness of graphene h=0.35 nm is negligibly small compared to H=25 μm. For this reason, the thermal resistance $R_\theta=L/(KhW)$ of the additional heat conduction channel via graphene will be much larger than via Cu film (here L is the length of the path). Thus, the high thermal conductivity of graphene [5] should not play a significant role in heat spreading ability of Cu foils over large distances (L~5 mm) if one considers conventional heat transfer by phonons. The observed enhancement of the apparent α and K can be understood if the thermal data is correlated with the microscopy data presented in Fig. 6.8.

One can see that CVD of graphene results in substantially stronger enlargement of Cu grains than annealing under the same conditions. The graphene CVD and annealing temperature 1030 ^{o}C is sufficiently larger than Cu recrystallization temperature of ~227 ^{o}C [23]. As a result, annealing accompanied by re-crystallization increases the grain sizes in Cu films, reduces the defect density and improves their mechanical properties [23-24]. Our results indicate that CVD of graphene enhances the Cu grain growth, as compared to

regular annealing, by changing the thermal balance during the deposition. Graphene also stops copper evaporation from the surface when the sample is heated during CVD. These conclusions are supported by earlier observations that the substrates and underlays affect the annealing process of Cu and the resulting Cu morphology [25]. It is also in agreement with the grain size data in Cu with CVD graphene and annealed Cu presented in Ref. [26]. Additionally, our SEM studies indicate that CVD of graphene results in ~20% reduction in surface roughness as compared to reference Cu.

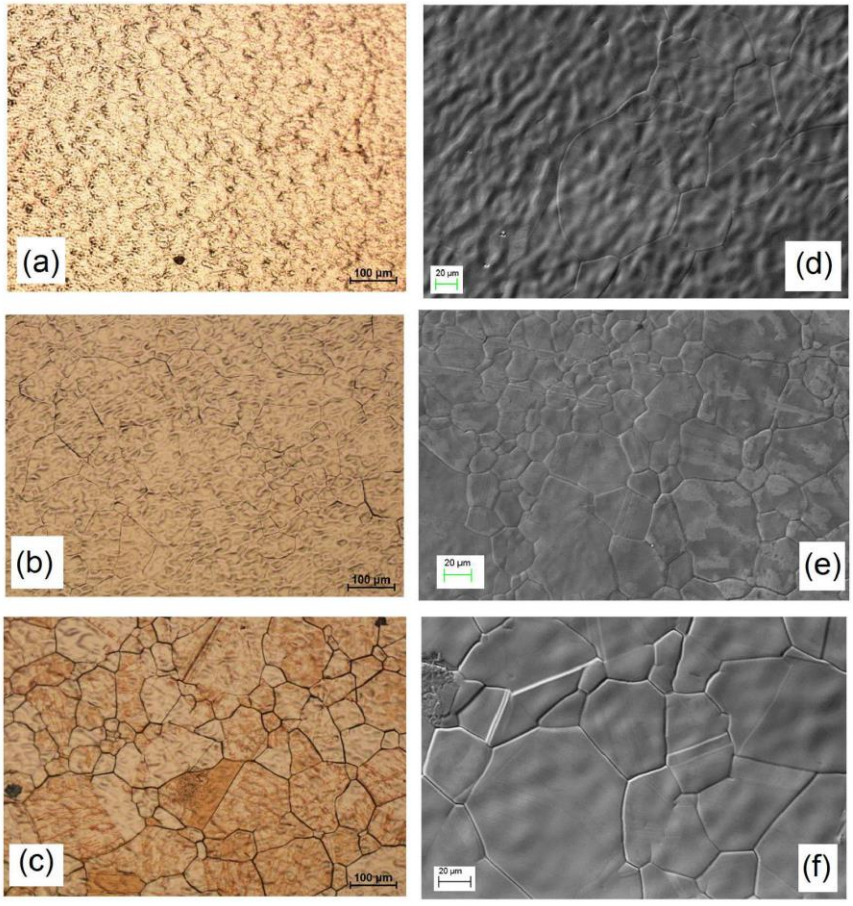

Fig. 6-7 . Optical image of the surface of Cu film (a); annealed Cu film (b); and Cu film with CVD graphene (c). SEM image of the surface of Cu film (d); annealed Cu film (e); and Cu film with CVD graphene (f). Note that deposition of graphene substantially increases the Cu grain size.

In order to further rationalize the experimental results we estimated the ratio of the average grain sizes, $\tilde{D}/D$, which would provide the relative change in the thermal conductivity, $\Delta K/K$, close to the one observed in the experiments ($\tilde{D}$ is typical grain size in reference Cu film and D is the grain size after CVD of graphene). The electron MFP for thermal transport is Λ=40 nm at RT [22]. Since $\Lambda << H$, it is reasonable to assume that K is mostly limited by the grain boundary scattering. In this case, one can express the thermal conductivity, K, of a polycrystalline metal through that of a single-crystal bulk metal, K_B, as [27-29] $K = (1+\Lambda/D)^{-1} K_B$. Applying this equation to polycrystalline Cu before and after CVD of graphene we derived the following relation

$$\frac{\tilde{D}}{D} = \frac{1-(\Delta K/K)}{1+(\Delta K/K)(D/\Lambda)}. \qquad (6.1)$$

It is well known that Cu films have very large distribution of grain sizes [24, 30]. It is common to have grain sizes within a given Cu sample varied by three orders of magnitude from tens of nm to tens of μm [30]. The shape of the grains in the Cu film can also be very anisotropic. Detail investigation of the grain size distribution requires expensive ion-milling and transmission electron microscopy study. For these reasons, here we provide simple estimates from the optical, SEM and AFM studies of our samples. If one assumes that the average grain diameters in Gr-Cu-Gr heterostructures

are in the range D≈1-10 μm, the experimentally measured $\Delta K/K$=0.2 can be achieved for $\tilde{D}/D$ ranging from ~0.13 to 0.016, which corresponds to the grains in reference Cu on the order of 130 – 160 nm. Note that the smaller grains can affect the thermal transport the most by limiting the heat carrier MFP. The considered range and change in the diameter by ×10-×100 after CVD is consistent with the microscopy data (see examples in Fig 6.7). It is known that annealing of Cu under different conditions can change the grain size by many orders of magnitude from ~30 nm to 100 mm [24]. Deposition of graphene can produce even stronger effect. Thus, our analysis suggests that the grain size increase can result in the observed enhancement of the thermal conductivity. Variations in the defect densities, e.g. dislocation lines, and grain boundary thickness after CVD of graphene may also affect the $\Delta K/K$.

In order to exclude a possibility that the change in thermal conductivity is due to the changes in the impurity content in Gr-Cu-Gr hetero-films and reference annealed Cu films we performed X-ray photoelectron spectroscopy (XPS) and energy-dispersive X-ray (EDX) spectroscopy inspection. It was established that the impurity composition (that included O and N) did not differ in graphene-Cu-graphene films with graphene and annealed Cu. The differences in the grain size and roughness of GCG-HF and those of annealed Cu films may also be related to differences in the oxidation process during and after CVD of graphene and annealing [31]. One should also note that graphene is an essential for improved thermal conductivity of Gr-Cu-Gr hetero-films. The experiments with deposition of amorphous carbon on Cu indicated that the thermal conductivity has

not increased but rather decreased. Amorphous carbon is known to have very low thermal conductivity of below 1 W/mK at RT [5].

We have also conducted four-probe electrical measurements in order to investigate if the observed change in thermal conductivity in Gr-Cu-Gr hetero-films follows the Wiedemann – Franz law [32] $K/\sigma=LT$, where σ is the electrical conductivity and $L=(\pi^2/3)(k_B/q)^2\approx 2.44\times10^{-8}$ WΩK^{-2} is the Lorenz number. The electrical conductivity of the samples was in line with the tabulated values for Cu films. However, it did not scale up linearly with the measured K as required by the Wiedemann – Franz law. We explain it by the fact that our samples are heterogeneous, and the electric probes pressed against Gr-Cu-Gr hetero-films contact both graphene or FLG layer and Cu. The electrical conductance is provided by both graphene and Cu channels. As a result, the evolution of electrical conductivity with the change in the grain size does not necessarily correlate well with the apparent thermal conductivity via the Wiedemann – Franz law.

Although it is clear that the observed strong enhancement of thermal properties of Cu films after CVD of graphene is mostly related to the effect produced by graphene on Cu grains one cannot completely exclude other possible mechanisms of heat conduction, which might be facilitated by graphene. It has been recently suggested theoretically that plasmons and plasmon-polaritons can strongly enhance the heat transfer in graphene and graphene-covered substrates [33-34]. The fact in our measurements the samples are heated by the light flash with the wide spectrum leaves this possibility open. The plasmon contribution would come in addition to the phonon heat conduction in graphene.

Our present findings add validity to the proposals of the graphene capped Cu interconnects by demonstrating improvement in their heat spreading ability. Taking into account that the next technology nodes will require Cu interconnects with the nm-range thickness [11] one can expect that the effects will be even more pronounced than in the examined □m-range thickness films. The latter may become a crucial consideration for electronic industry. In addition, our results can be possibly applied in metallurgy. Carbon additives have long been used in steel smelting as alloying elements distributed through the volume. Carbon alloying allows one to vary the hardness and strength of the metal [23]. Our results show that CVD of one-atom-thick graphene layer on the surface of metal foils can have a pronounced effect on its thermal properties. This is a conceptually different approach for the carbon use in metallurgy.

6.4. Theoretical Analysis Details

the equation for the thermal conductivity of polycrystalline material limited by the grain boundaries [27-29]:

$$K = (1 + \Lambda / D)^{-1} K_B . \quad (2)$$

Here D is the grain size (mean diameter), K_B is the thermal conductivity of bulk single-crystal material, Λ is the electron mean free path (MFP) for thermal transport, which can be larger than that for electrical transport [27-29]. Let us assume that the material with grain size D_1 has the thermal conductivity K_1 while the material with grain size D_2 has the

thermal conductivity K_2. We introduce two ratios: $\varsigma \equiv (\Delta K / K) = (K_2 - K_1)/K_2 = 1 - K_1/K_2$ and $\alpha = D_1 / D_2$. Writing Eq. (2) for two materials with two grain sizes D_1 and D_2, we get

$$K_1 = (1 + \Lambda / D_1)^{-1} K_B, \tag{3}$$

$$K_2 = (1 + \Lambda / D_2)^{-1} K_B. \tag{4}$$

Dividing Eq. (3) by Eq. (4), we can obtain for the thermal conductivity enhancement factor:

$$\varsigma = 1 - \frac{D_2 + \Lambda}{D_1 + \Lambda}\left(\frac{D_1}{D_2}\right) = 1 - \frac{D_2 + \Lambda}{\alpha D_2 + \Lambda}\alpha. \tag{5}$$

Solving Eq. (5) for α we get

$$\alpha = \frac{1 - \varsigma}{1 + D_2(\varsigma / \Lambda)} \tag{6}$$

Finally, we obtain the relation between the ratio of the grain sizes and increase in the thermal conductivity

$$\frac{D_1}{D_2} = \frac{1 - (\Delta K / K)}{1 + (\Delta K / K)(D_2 / \Lambda)} \tag{7}$$

The derived equation allows one to correlate the effect of increasing grain size in Cu films after graphene deposition with the measured increase in the thermal conductivity. Although the proposed model is simple it captures the main trend observed

experimentally. More accurate treatment requires inclusions of specifics of electron reflections from grain boundaries and external surfaces in polycrystalline films [35].

6.5. References

[1] Novoselov, K. S et al. Electric field effect in atomically thin carbon films. Science, 306, 666 (2004)

[2] Novoselov, K. S. et al. Two-dimensional gas of massless Dirac fermions in graphene. Nature, 438, 197-200 (2005)

[3] Kim, P. et al. Experimental observation of the quantum Hall effect and Berry's phase in graphene. Nature, 438, 201-204 (2005)

[4] Ghosh, S. et al. Dimensional crossover of thermal transport in few-layer graphene. Nature Mat., 9, 555-558 (2010)

[5] Balandin, A. A. Thermal properties of graphene and nanostructured carbon materials. Nature Mat., 10, 569-581 (2011)

[6] Lee, C. Wei, X. Kysar, J. W. & Hone, J. Measurement of the elastic properties and intrinsic strength of monolayer graphene. Science, 321, 385-388 (2008)

[7] X, Li et al. Large-area synthesis of high-quality and uniform graphene films on copper foils. Science, 324, 1312-1314 (2009)

[8] X, Li et al. Graphene films with large domain size by a two-step chemical vapor deposition process. Nano Lett., 10, 4328-4334 (2010)

[9] Mattevi, C. Kim, H. & Chhowalla, M. A review of chemical vapor deposition of graphene on copper. J. Mat. Chem., 21, 3324-3334 (2010)

[10] Kim, Y et al. Strengthening effect of single-atomic-layer graphene in metal–graphene nanolayered composites. Nature Comm., 4, 2114 (2013)

[11] Peercy, P. S. The drive to miniaturization. Nature, 406, 1023 (2000)

[12] Yu, J. Liu, G. Sumant, A. V. Goyal, V. & Balandin, A. A. Graphene-on-diamond devices with increased current-carrying capacity: Carbon sp^2-on-sp^3 technology. Nano Letters, 12, 1603 (2012)

[13] Kang, C. G. et al. Effects of multi-layer graphene capping on Cu interconnects. Nanotechnology, 24, 11, 115707 (2013)

[14] Yu, T. et. al. Bilayer graphene/copper hybrid on-chip interconnect: A reliability study. IEEE Transaction of Nanotechnology, 10, 4, 710 (2011)

[15] Chen, Z., et al. Three-dimensional flexible and conductive interconnected graphene networks grown by chemical vapour deposition. Nature Materials, 10, 424 (2011).

[16] Seol, J. H. et al. Two-dimensional phonon transport in supported graphene. Science, 328, 213-216 (2010)

[17] Calizo, I. et al. Ultraviolet Raman microscopy of single and multilayer graphene. J. Appl. Phys., 106, 43509 (2009)

[18] Parker, W. J. Jenkins, R. J., Butler, C. P. & Abbott, G. L. Flash method of determining Thermal diffusivity, heat capacity and thermal conductivity. J. Appl. Phys., 32, 1679 (1961)

[19] Young, H. D. & Freedman, R. A. University Physics: Table 17-5 (Addison-Wesley, 13th Edition 2013)

[20] Liu, W. Yang, Y. & Asheghi, M. Thermal and electrical characterization and modeling of thin copper layers. IEEE Transactions (2006) ISBN: 0-7803-9524-7, 1171-1176

[21] Nath, P. & Chopra, K. L. Thermal conductivity of copper films. Thin Solid Films, 20, 53 (1974)

[22] Przeliorz, R., Golar, M., Moskal, G. & Swadzba, L. The relationship between specific heat capacity and oxidation resistance of TiAl alloys. J. Achievements in Materials and Manufacturing Engineering, 21, 47 – 50 (2007)

[23] Flinn, R. A. & Trojan, P. K. Engineering Materials and Their Application: Effect of Stress and Temperature Fig. 3-26 (Houghton Mifflin Company, 1981)

[24] Gertsman, V. Y. et al. The study of grain size dependence of yield stress of copper for a wide grain size range. Acta Metall. Mater., 42, 10, 3539 (1994)

[25] Yang, J. Hunag, Y. & Xu, K. Effect of substrate on surface morphology evolution of Cu thin films deposited by magnetron sputtering. Surface and Coating Tech., 201, 5574 (2007)

[26] Bae, S. et al. Roll-to-roll production of 30-inch graphene films for transparent electrodes. Nature Nanotechnology, 5, 574–578 (2010)

[27] Qiu T. Q. and Tien, C.L. Size effects on nonequilibrium laser heating of metal films J. Heat Transfer, 115, 842 (1993)

[28] Kumar, S. & Vradis, G.C. Thermal conductivity of thin metallic films. J. Heat Transfer, 116, 28 (1994)

[29] Zhang, Q.S. et al. Size effects on the thermal conductivity of polycrystalline platinum nanofilms. J. Phys.: Condens. Matt, 18, 7937 (2006)

[30] Zielinski, E.M., Vinci, R.P. & Bravman, J.C. Effects of barrier layer and annealing on abnormal grain growth in copper thin films, J. Appl. Phys., 76, 4516 (1994)

[31] Kidambi, P.R. et al., Observing graphene grow: catalyst-graphene interactions during scalable graphene growth on polycrystalline copper. Nano Lett., 13, 4769 (2013)

[32] Franz, R., Wiedemann, G. Ueber die Wärme-Leitungsfähigkeit der Metalle, Annalen der Physik (in German) 165, 497 (1853).

[33] Svetovoy, V.B. VanZwol, P. J. & Chevrier, J. Plasmons enhance near-field radiative heat transfer for graphene-covered dielectrics. Phys. Rev. B, 85, 155418 (2012)

[34] Ilic, O., et al. Near-field thermal radiation transfer controlled by plasmons in graphene. Phys. Rev. B, 85, 155422 (2012)

[35] Mayadas, A.F. & Shatzkes, M. Electrical-resistivity model for polycrystalline films: the case of arbitrary reflection at external surfaces. Phys. Rev. B, 1, 1382 (1970).

Chapter VII

Conclusions

7.1. Summary of Dissertation

In conclusion, we demonstrated that the use of graphene and few-layer graphene as fillers in organic phase change material allows one to increase its thermal conductivity by more than two orders of magnitude while preserving its latent heat storage ability. The strong enhancement is achieved via easy binding of graphene flakes to paraffinic hydrocarbons resulting in good thermal coupling. The exceptionally large thermal conductivity of graphene improves the heat conduction ability of paraffins. It was also shown through measurements and computer simulations that improved thermal properties of graphene PCM result in significant temperature rise inside realistic Li-ion battery packs. The described combined heat storage–heat conduction approach may lead to a transformative change in thermal management of batteries. We reported the thermal properties of Li-ion battery electrodes enhanced with multi-wall CNTs. The electrodes were synthesized via an inexpensive scalable *filtration* method. Our measurements indicate that the CNT enhanced electrodes reveal up to *two-orders-of-magnitude* enhancement of the thermal conductivity. The in-plane thermal conductivity in some electrodes reached ~141 W/mK at RT. The described approach for increasing the thermal conductivity can be extended to commercial electrode-active materials. The obtained results are important for thermal management of Li-ion and other high-power-density batteries. we demonstrated experimentally that graphene – Cu – graphene heterogeneous films reveal strongly enhanced thermal conductivity as compared to the reference Cu and annealed Cu films. Chemical vapor deposition of graphene on both sides of 9-μm-thick Cu films increases their thermal conductivity by up to 24% near room temperature. The effect of graphene is

projected to be substantially stronger in nm-thick Cu interconnects. The observed improvement of thermal properties of graphene – Cu – graphene hetero-films results primarily from the changes in Cu morphology during graphene deposition. Enhancement of thermal properties of graphene capped Cu films is important for thermal management of advanced electronic chips, and adds validity to the proposed applications of graphene in the hybrid graphene – Cu interconnects. Our results indicating that deposition of just one atomic plane of graphene on a surface can substantially improve the properties of underlying metal film may lead to a transformative change for the use of carbon in metallurgy.

7.2. Competitive Awards Won During the Dissertation Research

- Recipient of Dean's Distinguished Fellowship award, Bourns College of Engineering (2010).
- University of California Riverside (2010-2011).
- Recipient of Best Teaching Assistant Award June (2011).
- Recipient of Dean's Dissertation Year Program Fellowship (2013 – 2014)

7.3. Peer-Reviewed Journals Published from Dissertation Research

1. P. Goli, X. Li, C. Y. Lu, K. S. Novoselov and A. A. Balandin, Strong Enhancement of Thermal Properties of Copper Films after Chemical Vapor Deposition of Graphene", Accepted Nanoletters, ASAP, 2014.

2. P. Goli, B. Koo, A. Sumant, C. D. S. Carlo, T. Rajh, C. Johnson, A. A. Balandin and E. V. Shevchenko, "Carbon-Nanotube Enhanced Li- Ion Battery Electrodes with Signicantly Increased Thermal Conductivity" 2014, Submitted to Carbon.

3. W. Wang, P. Goli, J. Alaniz, Z. Whang, J. Shi, J. E. Garey, A. A. Balandin and Y. Yin. "High figure-of-merit of nanostructured bulk thermo-electrics with lamellar ordering" 2014, Submitted to Nature Materials.

4. P. Goli and A. A. Balandin, "Graphene-Enhanced Phase Change Materials for Thermal Management of Battery Packs", IEEE ITHERM 2014.

5. P. Goli, S. Legedza, A. Dhar, R. Salgado, J. Renteria and A. A. Balandin, "Graphene-enhanced hybrid phase change materials for thermal management of Li-ion batteries", Journal of Power Sources 248 (1), 37 (2014).

6. P.Goli, J. Khan, D. Wickramaratne, R. K. Lake and A. A. Balandin, "Charge Density Waves in Exfoliated Films of van der Waals Materials: Evolution of Raman Spectrum in TiSe2 ", 12, 11, 5941-5945 (2012).

7. P. Goli and A. A. Balandin, "Graphene Applications in Phase Change Materials for Thermal Management of High-Power Density Battery Packs", SRC Techcon,P067012, (2013).

8. P. Goli, "CurrentVoltage Characteristics of Graphene Nanoribbons in the Ballistic Transport Regime", Journal of Nano Electronics and Optoelectronics, 7, 4, 381, 2012.

9. J. Renteria, G. Liu, Z. Hossain, C. Jiang, R. Samnakay, Z. Yan, P. Goli and A. A. Balandin, "Low-frequesncy 1/f noise in Graphene: Effects ofIrradiation, Temperature, and Thickness Scaling", SRC Techccon, 11.7,Ausitn, TX September 2013.

10. J. Renteria, R. Samnakay, C. Jiang, T.R. Pope,P. Goli, Z. yan, D. Wickramaratne, T. T. Salguero, A. G. Khitun, R. K. Lake and A. A. Balandin, "All-metallic electrically gated 2H-TaSe2 thin-film switches and logic circuits", 115, 3, 34305 (2014).

11. J. Renteria, R. Samnakay, S. L. Rumyantsev, P. Goli, M. S. Shur and A. A. Balandin, "Low-Frequency 1/f Noise in Molybdenum Disulfide Transistors" (2014), Submitted to Journal of Applied Physics.

12. Z. Yan, C. Jaing, T. R. Pope, C. F. Tsang, J. L. Stickney, P. Goli, J. Renteria, T. T. Salguero and A. A. Balandin, "Phonon and thermal properties of exfoliated TaSe2 thin films", Journal of Applied Physics, 114, 201 204301 (2013).

7.4. Conference presentation from the dissertation research

1. P. Goli and A. A. Balandin, "Graphene-Enhanced Phase Change Materials for Thermal Management of Battery Packs", IEEE ITHERM, Orlando, FL, May (2014).

2. P. Goli, S. Legedza, A. Dhar, R. Salgado, J. Renteria and A. A. Balandin, "Graphene Enhanced Phase Change Materials for Thermal Management of High-Power Density Battery Packs", MRS Spring Meet, Q3.04, San Francisco, CA, April (2014).

3. P. Goli, H. Ning, X. Li, C. Yu, K. S. Novoselov and A. A. Balandin, "Strong Increase of the Thermal Conductivity of Copper Films after Chemical Vapor Deposition of Graphene", MRS Spring Meet, OO4.02, San Francisco, CA, April (2014).

4. H. Malekpur, P. Goli, C. P. Lai, K. H. Chang, H. Ning, X. Li, C. Yu, K. S. Novoselov and A. A. Balandin, "Thermal Conductivity Measurements of Graphene Laminate Films on PET Substrate Using the Raman Optothermal Method", MRS Spring Meet, OO10.03, San Francisco, CA, April (2014).

5. J. Renteria, R. Samnakay, Z. Yan, C. Jiang, T. R. Pope, P. Goli T. T. Salguero and A. A. Balandin, "Electrical Switching Phenomena in Tantalum Diselenide Thin-Film Devices", MRS Spring Meet, NN5.09, San Francisco, CA, April (2014).

6. P. Goli and A. A. Balandin, "Grapheen Thermal Properties and Applications for Thermal Management", Graphene Commercialization and Application, San Francisco, CA December (2013). (Invited Speaker)

7. P. Goli and A. A. Balandin, "Phonon Engineering and Phononic Devices: From Nanowires and Quantum Dots to Graphene and Van der Waals Materials" ASME IMECE, IMECE 2013-66108, San Diego, CA (2013).

8. P. Goli, S. Legedza and A. A. Balandin, "Graphene Thermal Properties and Applications for Thermal Management of Li-Ion Batteries" AVS 60 Technical Exhibition and Program, GR+AS+EM+MI+MN+TuM2, Long Beach, CA, October (2013).

9. J. Renteria, G. Liu, Z. Hossain, C. Jiang, R. Samnakay, Z. Yan, P. Goli and A. A. Balandin, "Low-frequency 1/f noise in Graphene: Effects of Irradiation, Temperature, and Thickness Scaling", SRC Techccon, 11.7, Ausitn, TX September 2013.

10. P. Goli and A. A. Balandin, "Graphenes Applications in Phase Change Materials for Thermal Management of Li-Ion Batteries", SRC Techccon, 11.7, Ausitn, TX September 2013.

11. P. Goli and A. A. Balandin, " Graphene Thermal Properties and Applications for Thermal Management", Graphene Commercialization and Application, London, UK June (2013). (Invited Speaker).

12. P. Goli and A. A. Balandin, "Graphene Thermal Properties and Applications for Thermal Management", Advancements in Thermal Management, Denver, CO June (2013). (Keynote Speaker).

13. P. Goli and A. A. Balandin, " Graphene Fillers in Phase-Change Materials for Thermal Management of Li-Ion Batteries", Graphene Week, GW2013- 115, Chemnitz, Germany, June 2013.

14. P. Goli and A. A. Balandin, "Graphene Thermal Properties and Applications for Heat Removal in the Phase Change Materials", ECS 223rd Meeting, 751, Toronto, Canada, May 2013. (Invited Talk).

15. D. Wickramaratne, P. Goli, A. A. Balandin and R. Lake, "The effect of dimensionality on the charge-density-wave phase in layered dichalcogenides", APS March Meeting, Y19.00003, 2013.

16. P. Goli and A. A. Balandin, "Nominated for Outstanding Research in Energy" World Technology Network Awards Summit, New York, October 2012.

17. P. Goli and A. A. Balandin, "Graphene Based Thermal Interface Materials", ECS PRiME, 3476, Honolulu, HI, October 2012.

18. D. L. Nika, A. Askerov, P. Goli and A. A. Balandin, "Thermal Conductivity of Graphene Ribbons: Non-Monotonic Size Dependence", ECS PRiME, 3480, Honolulu, HI, October 2012.

7.5. Poster Presentations form this Dissertation research

1. R. R. Samnakay, J. Renteria, C. Jiang, T. R. Pope, Z. Yan, P. Goli, M. Stolyerov, T. T. Salguero and A. A. Balandin, "Optical Switching Phenomena in Tantalum Diselenide Thin Films", MRS Spring, NN3.43, 2014.

2. C. Jiang, Z. Yan, T. R. Pope, C. T. Tsang, J. L. Stickney, P. Goli,J. Renteria, T. T. Salguero and A. A. Balandin. "Thermal and Phonon Properties of Exfoliated TaSe2 Thin Films", MRS Spring, NN3.05, Spring 2014.

3. J. renteria, Z. Yan, R. Samnakay, P. Goli, C. Jiang, "Electron and Phonon Transport in Field-Effect Devices with 2H-TaSe2 Thin-Film Channels", FAME Research Review, Losa Angeles, CA, Nov 2013.

4. J. Renteria, R. Samnakay, Z. Yan, P. Goli, C. Jiang and A. A. Balandin, "Photoconduction in Two-Dimensional Charge-Density-Wave Materials:Applications in Optical Detectors", ISANN, PI-4, Poipu Beach, Kauai, 2013.

5. P. Goli, S. Legedza, J. Renteria, Z. Yan, A. Dhar, R. Salgado and A. A. Balandin, "Engineering Thermal Transport in Composites with Graphene and Multilayer Graphene Fillers", SRC Techcon, 11.7, Ausitn, TX September 2013.

6. J. Renteria, G. Liu, Z. Hossain, C. Jiang, R. Samnakay, Z. Yan, P. Goli and A. A. Balandin, "Low-frequesncy 1/f noise in Graphene: Effects of Irradiation, Temperature, and Thickness Scaling", SRC Techccon, 11.7, Ausitn, TX September 2013.

7. P. Goli and A. A. Balandin. "Engineering thermal transport in composites with graphene and multilayer graphene fillers", cecam Nanophononics, Bremen, Germany, Aug 2013.

8. P. Goli, D. L. Nika and A. A. Balandin, "Folded and entangled phonons in twisted bilayer graphene: engineering phonons by atomic plane rotations", cecam Nanophononics, Bremen, Germany Aug 2013.

9. C. Jiang, R. Samnakay, Z. Yan, J. Renteria,, S. Ramirez, P. Goli and A. A. Balandin, "Microscopic and Raman Characterization of TaSe2 and TaS2, Films in Normal and Charge-Density Wave Regime", NRI review, June 2013.

10. P. Goli, Z. Yan, G. Liu and A. A. Balandin, "Graphene Quilts for Heat Removal from High-Power GaN Transistors ", GW2013-213.

11. P. Goli, S. Legedza, A. Dhar, R. Salgado, R. Gulotty and A. A. Balandin, "Comparative Testing of Thermal Interface Materials under Realistic Conditions"

MRS Spring meet, E6.13 2013.

12. P. Goli, J. Renteria, R. S. Gulotty, S. Ramirez, Z. Yan, m. Micklich, R. R. Samnakay, C. Jiang and A. A. Balandin, "Phonon Engineering and Energy Conversion in Van der Waals Materials", FAME Research Review, Los Angeles, CA, Feb 2013.

13. P. Goli and A. A. Balandin, "Charge Density Waves in Exfoliated Films of Van der Waals Material: Evolution of Raman Spectrum in TiSe2 ", NRI Review, UC Riverside, August 2013.

14. P. Goli and A. A. Balandin, "Simulation of Electron Transport in Nanoscale Graphene Devices", MRS Spring, EE8.1, 2012.

15. P. Goli, J. M. Khan and A. A. Balandin, "Thermal Management of Li-Ion Batteries with Nanostructured Carbon Electrodes", MRS Spring Meet O9.93 2012.

16. G. Liu, M. Rahman, P.Goli and Alexander A. Balandin "Low-Noise Top- Gate Graphene Transistors", DARPA/SRC MARCO FENA Research Review, Los Angeles, CA, January 26, 2010.

17. M.Rahman, I.Bejenari, D.Kotchetkov, V.Goyal, M.Z.Hossain, C.Nolen, K.M.F Shahil, P.Goli and A.A.Balandin, "Mobility in Silicon and Poly- Silicon channels embedded with acoustically hard polycrystalline diamond barriers", DARPA/SRC MARCO FENA Research Review, Los Angeles, CA, January 27, 2009.